

# SDSS DR7 superclusters

## Morphology

M. Einasto<sup>1</sup>, L. J. Liivamägi<sup>1,2</sup>, E. Tago<sup>1</sup>, E. Saar<sup>1</sup>, E. Tempel<sup>1,2</sup>, J. Einasto<sup>1</sup>, V. J. Martínez<sup>3</sup>, and P. Heinämäki<sup>4</sup>

<sup>1</sup> Tartu Observatory, 61602 Tõravere, Estonia  
e-mail: maret@aai.ee

<sup>2</sup> Institute of Physics, Tartu University, Tähe 4, 51010 Tartu, Estonia

<sup>3</sup> Observatori Astronòmic, Universitat de València, Apartat de Correus 22085, 46071 València, Spain

<sup>4</sup> Tuorla Observatory, University of Turku, Väisäläntie 20, Piikkiö, Finland

Received 24 January 2011 / Accepted 2 May 2011

### ABSTRACT

**Aims.** We study the morphology of a set of superclusters drawn from the SDSS DR7.

**Methods.** We calculate the luminosity density field to determine superclusters from a flux-limited sample of galaxies from SDSS DR7 and select superclusters with 300 and more galaxies for our study. We characterise the morphology of superclusters using the fourth Minkowski functional  $V_3$ , the morphological signature (the curve in the shapefinder's  $K_1$ - $K_2$  plane) and the shape parameter (the ratio of the shapefinders  $K_1/K_2$ ). We investigate the supercluster sample using multidimensional normal mixture modelling. We use Abell clusters to identify our superclusters with known superclusters and to study the large-scale distribution of superclusters.

**Results.** The superclusters in our sample form three chains of superclusters; one of them is the Sloan Great Wall. Most superclusters have filament-like overall shapes. Superclusters can be divided into two sets; more elongated superclusters are more luminous, richer, have larger diameters and a more complex fine structure than less elongated superclusters. The fine structure of superclusters can be divided into four main morphological types: spiders, multispiders, filaments, and multibranching filaments. We present the 2D and 3D distribution of galaxies and rich groups, the fourth Minkowski functional, and the morphological signature for all superclusters.

**Conclusions.** Widely different morphologies of superclusters show that their evolution has been dissimilar. A study of a larger sample of superclusters from observations and simulations is needed to understand the morphological variety of superclusters and the possible connection between the morphology of superclusters and their large-scale environment.

**Key words.** cosmology: observations – large-scale structure of Universe – galaxies: clusters: general

## 1. Introduction

The most remarkable feature of the megaparsec-scale matter distribution in the Universe is the presence of the cosmic web – the network of galaxies, groups, and clusters connected by filaments (Joeveer et al. 1978; Gregory & Thompson 1978; Zeldovich et al. 1982; de Lapparent et al. 1986). The formation of a web of galaxies and systems of galaxies is predicted in any physically motivated theory of the formation of structure in the Universe (see, e.g., Bond et al. 1996). In this scenario galaxies and galaxy systems form because of initial density perturbations on different scales. Perturbations on a scale of about  $100 h^{-1}$  Mpc ( $H_0 = 100 h \text{ km s}^{-1} \text{ Mpc}^{-1}$ ) give rise to the largest systems of galaxies – rich superclusters. At larger scales dynamical evolution proceeds at a slower rate and superclusters have retained the memory of the initial conditions of their formation and of the early evolution of structure (Einasto et al. 1980; Zeldovich et al. 1982; Kofman et al. 1987).

Numerical simulations show that high-density peaks in the density distribution (the seeds of supercluster cores) are seen already at very early stages of the formation and evolution of structure (Einasto 2010). These are the locations of the formation of the first objects in the Universe (e.g. Venemans et al. 2004; Mobasher et al. 2005; Ouchi et al. 2005). Observations have already found superclusters at high redshifts (Nakata et al. 2005; Swinbank et al. 2007; Gal et al. 2008; Tanaka et al. 2009).

Recently, the *XMM-Newton* satellite follow-up for the validation of Planck cluster candidates led to the discovery of two massive, previously unknown superclusters of galaxies (Planck Collaboration et al. 2011). These are likely the first superclusters discovered through the Sunyaev-Zeldovich effect.

Superclusters are important tracers of dark and baryonic matter in the Universe (Zappacosta et al. 2005; Génova-Santos et al. 2005; Heymans et al. 2008; Buote et al. 2009; Padilla-Torres et al. 2009; Schirmer et al. 2011). Studies of superclusters and of the supercluster-void network have demonstrated the presence of a characteristic scale in the distribution of rich superclusters (Einasto et al. 1994, 1997a). This was probably an early hint of baryon acoustic oscillations (Hütsi 2010).

To search for superclusters and to understand their properties, we need to know how to identify them and how to quantify their properties (Bond et al. 2010). Several methods have been proposed to study the cosmic web (Bharadwaj et al. 2004; Stoica et al. 2010; Aragón-Calvo et al. 2010; Sousbie 2011; Sousbie et al. 2011, and references therein). One approach is to determine cosmic structures (in our study – superclusters of galaxies) using the density field and to study their morphology with Minkowski functionals and shapefinders (Schmalzing & Buchert 1997; Sathyaprakash et al. 1998; Basilakos 2003; Sheth et al. 2003; Shandarin et al. 2004; Einasto et al. 2007d, and references therein). Oort (1983) gave a review of the early studies of superclusters. Supercluster catalogues compiled based on data

about clusters of galaxies were published by [Zucca et al. \(1993\)](#); [Einasto et al. \(1994\)](#); [Kalinkov & Kuneva \(1995\)](#); [Einasto et al. \(2001\)](#). Recent deep surveys of galaxies (as 2dFGRS and SDSS, see [Colless et al. 2003](#); [Abazajian et al. 2009](#)) introduced a new era in the studies of the large-scale structure of the Universe, where systems of galaxies can be studied in unprecedented detail. A number of supercluster catalogues have been compiled with these data ([Basilakos 2003](#); [Einasto et al. 2003a](#); [Erdođdu et al. 2004](#); [Einasto et al. 2006, 2007b](#); [Liivamägi et al. 2010](#); [Luparello et al. 2011](#), and references therein).

The overall morphology of superclusters has been studied by several authors ([Kolokotronis et al. 2002](#); [Basilakos 2003](#); [Costa-Duarte et al. 2011](#)), we refer to [Einasto et al. \(2007a\)](#) for a review of the properties of superclusters. The shapes and sizes of superclusters can be used to compare the observed superclusters with those obtained from cosmological simulations ([Kolokotronis et al. 2002](#); [Einasto et al. 2007a](#)). [Nichol et al. \(2006\)](#) showed that the higher order correlation functions of the 2dFGRS do not agree with those found in numerical simulations (but this fact can be explained by non-Gaussian initial density fields, [Gaztanaga & Maehoenen 1996](#)). This discrepancy may be caused by the unusual morphology of one of the richest superclusters in the 2dFGRS, the supercluster SCI 126 ([Einasto et al. 2007d, 2008](#)) from the catalogue of superclusters by [Einasto et al. \(2001, hereafter E01\)](#). The morphology of superclusters may be used to distinguish between different cosmological models ([Kolokotronis et al. 2002](#)).

Superclusters contain structures with a wide range of densities, from high-density cores of rich clusters to low-density filaments between clusters and groups. This makes them ideal laboratories to study processes that affect the evolution of galaxies, groups, and clusters of galaxies. A number of studies have already shown that the supercluster environment affects the properties of galaxies, groups, and clusters located there ([Einasto et al. 2003b](#); [Plionis 2004](#); [Wolf et al. 2005](#); [Haines et al. 2006](#); [Einasto et al. 2007c](#); [Porter et al. 2008](#); [Tempel et al. 2009](#); [Fleener & Johnston-Hollitt 2010](#); [Tempel et al. 2011](#); [Einasto et al. 2011](#)). Other evidence about the influence of the large-scale environment of galaxies on their properties comes from the study of the properties of galaxies in void walls ([Ceccarelli et al. 2008](#)) and from the study of the large-scale environment of quasars ([Lietzen et al. 2009](#)). A detailed information on the morphology of superclusters is needed to find out whether that may also be an important environmental factor in shaping the properties of galaxies and groups of galaxies in superclusters (see also [Aragón-Calvo et al. 2010](#)).

[Einasto et al. \(2007d\)](#) showed that the morphology of a typical poor supercluster can be described as a “spider” – a system of several filaments growing from one concentration centre (a rich cluster). The Local Supercluster is an example of a typical “spider”. Rich superclusters can be described as “multispiders”, where several high-density clumps are connected by lower-density filaments. One very rich supercluster (SCI 126) was described as a multibranching filament that consists of a rich filament of a quite uniform high density with poorer filaments for branches. This work concerned only a few of the richest supercluster while the present analysis enables us to test the classification of the morphology of superclusters.

The goal of the present paper is to study in detail the morphology of a large sample of superclusters drawn from the 7th data release of the Sloan Digital Sky Survey (SDSS). The superclusters are determined using the global luminosity field and their morphologies are quantified with the Minkowski functionals and shapefinders. The superclusters are divided into two

sets using multidimensional normal mixture modelling, applying the *Mclust* package for clustering and classification ([Fraleay & Raftery 2006](#)) from *R*, an open-source free statistical environment developed under the GNU GPL ([Ihaka & Gentleman 1996](#), <http://www.r-project.org>). The cluster membership of superclusters and their large-scale distribution is analysed, and a short description of individual superclusters is given. The data are described in Sect. 2, the methods in Sect. 3, and the results in Sect. 4. In Sect. 5 the selection effects in our sample are discussed, and a comparison with other studies is given. The study is summarised in Sect. 6. Interactive 3D models of the richest superclusters in our sample can be found on our web page: <http://www.aai.ee/~maret/SDSSsclmorph.html>.

We assume the standard cosmological parameters: the Hubble parameter  $H_0 = 100 h \text{ km s}^{-1} \text{ Mpc}^{-1}$ , the matter density  $\Omega_m = 0.27$ , and the dark energy density  $\Omega_\Lambda = 0.73$ .

## 2. Data

We selected the MAIN galaxy sample of the 7th data release of the Sloan Digital Sky Survey ([Adelman-McCarthy et al. 2008](#); [Abazajian et al. 2009](#)) with the apparent  $r$  magnitudes  $12.5 \leq r \leq 17.77$ , excluding duplicate entries. The sample is described in detail in [Tago et al. \(2010, hereafter T10\)](#). We corrected the redshifts of galaxies for the motion relative to the CMB and computed the co-moving distances ([Martínez & Saar 2002](#)) of galaxies.

The absolute magnitudes of galaxies are determined in the  $r$ -band  $M_r$  with  $k$ -correction for the SDSS galaxies calculated with the KCORRECT algorithm ([Blanton et al. 2003a](#); [Blanton & Roweis 2007](#)). In addition, we applied the evolution corrections, using the luminosity evolution model of [Blanton et al. \(2003b\)](#). The magnitudes correspond to the rest-frame at the redshift  $z = 0$ .

The first step is to determine groups and clusters of galaxies with the friends-of-friends algorithm, where a galaxy belongs to a group of galaxies if this galaxy has at least one group member galaxy closer than the selected linking length. The linking length along with the distance was increased, to take into account selection effects, when constructing a group catalogue for a flux-limited sample. As a result, the maximum sizes and velocity dispersions of groups are similar at all distances. For details and for the group catalogue we refer the reader to T10<sup>1</sup>.

To determine the luminosities of groups and to calculate the luminosity density field we have also to correct for the luminosities of galaxies that lie outside of the survey magnitude range. The calculation of luminosities is described in Appendix A (details of this calculation are given also in [Tempel et al. 2011](#)).

In the final flux-limited group catalogue the richness of groups decreases rapidly at distances  $D > 320 h^{-1} \text{ Mpc}$  because of selection effects. This effect is seen in Fig. 1. At small distances,  $D < 70 h^{-1} \text{ Mpc}$  luminosity weights are large owing to the absence of very bright galaxies. Therefore we chose for the present analysis a subsample of galaxies and galaxy systems in the distance interval  $90 h^{-1} \text{ Mpc} \leq D \leq 320 h^{-1} \text{ Mpc}$  where the selection effects are small.

We calculated the smoothed luminosity density field of galaxies and determined extended systems of galaxies (superclusters) using this density field. To determine superclusters,

<sup>1</sup> The T10 group catalogue is available in electronic form at the CDS via anonymous ftp to [cdsarc.u-strasbg.fr](mailto:cdsarc.u-strasbg.fr) (130.79.128.5) or via <http://cdsarc.u-strasbg.fr/viz-bin/qcat?J/A+A/514/A102>.

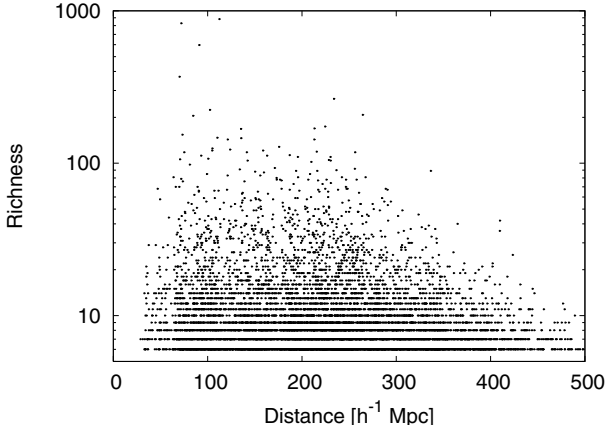


**Fig. 1.** Richness of groups vs. their distance in the T10 group catalogue. Only the data for groups with at least six member galaxies are plotted. This plot shows that at distances larger than  $\approx 320 h^{-1}$  Mpc almost no rich group is visible.

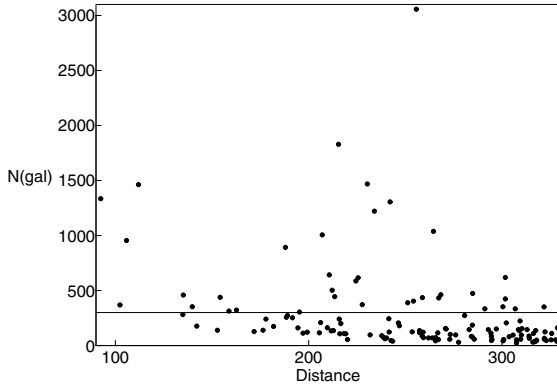


**Fig. 2.** Richness of superclusters vs. their distance (in Mpc/h). The line marks the value  $N_{\text{gal}} = 300$ .

we created a set of density contours by choosing a series of density thresholds. We define connected volumes above a certain density threshold as superclusters. Different threshold densities correspond to different supercluster catalogues. In order to choose proper density levels to determine individual superclusters, we analysed the density field superclusters at a series of density levels. The mean luminosity density of our sample is  $\ell_{\text{mean}} = 1.526 \times 10^{-2} \frac{10^{10} h^{-2} L_{\odot}}{(h^{-1} \text{Mpc})^3}$ . We chose the density level  $D = 5.0$  (in the units of mean density) to determine individual superclusters. At this density level superclusters in the richest chains of superclusters in the volume under study still form separate systems; at lower density levels they merge into huge percolating systems. At higher threshold density levels superclusters are smaller and their number decreases. Details of the calculation of the luminosity density field and of the supercluster catalogue are given in Appendix A and in Liivamägi et al. (2010).

Figure 2 shows the richness of superclusters vs. their distance. At distances less than  $200 h^{-1}$  Mpc there are only a few superclusters with less than 300 member galaxies. This selection effect is owed to the sample geometry – it is a pyramid with the top at the location of the observer. At the distance of  $100 h^{-1}$  Mpc the size of the base is  $220 \times 140 h^{-1}$  Mpc only, and it contains only a few superclusters. At distances between 100 and  $200 h^{-1}$  Mpc the number of superclusters is small – there is a void region between the nearby superclusters and those at

distances larger than  $200 h^{-1}$  Mpc (we will describe the large-scale distribution of superclusters in Sect. 4). To avoid these selection effects and to be able to resolve the details of supercluster’s density distribution (their morphology), we chose all superclusters in our distance interval with at least 300 observed member galaxies; Fig. 2 shows that they are present at all distances. Data of these superclusters are given in Table 1. In this table superclusters are ordered as they are presented in the text below: first the data of the superclusters with at least 950 member galaxies, and then of the superclusters with less members. Throughout the paper we use the supercluster ID numbers from the L10 catalogue ( $SCl_{\text{ID}}$  in Table 1).

To make the calculations of morphology insensitive to selection corrections, we work with volume-limited samples and the number density of galaxies instead of flux-limited samples and luminosity density. We recalculated the density field for each individual supercluster with a kernel estimator with a  $B_3$  box spline as the smoothing kernel, with the radius of  $8 h^{-1}$  Mpc (for details we refer to Saar et al. 2007; Einasto et al. 2007d), and volume-limited samples of individual superclusters. The absolute magnitude limits and the numbers of galaxies in the volume-limited versions of superclusters are given in Table 1.

### 3. Methods

#### 3.1. Minkowski functionals and shapefinders

The supercluster geometry (morphology) is defined by its outer (limiting) isodensity surface and its enclosed volume. The morphology of the isodensity contours is (in the sense of global geometry) completely characterised by the four Minkowski functionals  $V_0 - V_3$  (we give the formulas in Appendix B). For a given surface the four Minkowski functionals (from the first to the fourth) are proportional to the enclosed volume  $V$ , the area of the surface  $S$ , the integrated mean curvature  $C$ , and the integrated Gaussian curvature  $\chi$ . The last of them, the fourth Minkowski functional  $V_3$ , describes the surface topology; it is a sum of the number of isolated clumps and the number of void bubbles minus the number of tunnels (voids open from both sides) in the region (see, e.g. Saar et al. 2007). High values of the fourth Minkowski functional  $V_3$  suggest a complicated (clumpy) morphology of a supercluster.

For the argument labelling the isodensity surfaces, we use the (excluded) mass fraction  $mf$  – the ratio of the mass in regions with lower density than at the surface, to the total mass of the supercluster. The value  $mf = 0$  corresponds to the whole supercluster, and  $mf = 1$  to its highest density peak.

With the fourth Minkowski functional  $V_3$  we describe the clumpiness of the galaxy distribution inside superclusters – the fine structure of superclusters. When the density level is higher than the value used to determine a supercluster, the isodensity surfaces move from the outer regions of a supercluster into its central regions (the value of the mass fraction runs from 0 to 1). Therefore some galaxies in the outer regions of a supercluster do not contribute to the supercluster any more and this changes the inner morphology of the supercluster, which is reflected in the  $V_3 - mf$  relation (the number of isolated clumps changes, void bubbles, and tunnels may appear inside superclusters). We calculate  $V_3$  for superclusters for a range of threshold densities (mass fractions), starting with the lowest density that determines superclusters ( $mf = 0$ ), up to the peak density in the supercluster core ( $mf = 1$ ). In Sect. 4.2 we present figures showing the fourth Minkowski functional  $V_3$  for the whole threshold density

**Table 1.** Data of the superclusters.

(1)	(2)	(3)	(4)	(5)	(6)	(7)	(8)	(9)	(10)	(11)	(12)	(13)	(14)
$SCl_{ID}$	$ID_{E01}$	ID	$N_{gal}$	$N_{30}$	$d_{peak}$ Mpc/h	$L_{tot}$ $10^{10} h^{-2} L_{\odot}$	Diam. Mpc/h	$R_{magV}$ mag	$N_{galV}$	$V_{3,max}$	$K_1$	$K_2$	$K_1/K_2$
1	162	239+027+009	1038	4	264.5	1591.5	50.3	-19.70	916	2	0.077	0.163	0.48
10	160	239+016+003	1463	2	111.9	680.2	22.8	-17.50	1455	1	0.026	0.024	-
11	154	227+006+007	1222	5	235.0	1476.0	35.4	-19.30	1180	3	0.051	0.056	0.92
24	111	184+003+007	1469	4	230.4	1768.2	56.4	-19.25	1419	6	0.077	0.163	0.48
55	111	173+014+008	1306	4	242.0	1773.0	50.3	-19.55	1155	5	0.084	0.198	0.43
60	160	247+040+002	1335	3	92.0	527.4	21.2	-17.30	1275	1	0.010	0.020	-
61	126	202-001+008	3056	15	255.6	4315.3	107.0	-19.25	3048	13	0.130	0.460	0.28
94	158	230+027+006	1830	10	215.4	2263.4	54.6	-19.40	1632	9	0.110	0.399	0.28
336	109	172+054+007	1005	6	170.0	1003.6	53.3	-19.30	832	4	0.081	0.250	0.33
350	160	230+008+003	955	5	105.8	436.3	23.0	-17.50	947	2	0.029	0.045	0.65
38	95	167+040+007	586	5	224.4	660.7	22.5	-19.40	507	2	0.028	0.033	0.84
64	164	250+027+010	619	2	301.7	1305.4	55.7	-19.70	618	3	0.087	0.230	0.38
87	-	215+048+007	445	1	213.4	477.8	21.6	-19.00	445	2	0.036	0.033	1.09
136	271	189+017+007	504	5	212.1	523.2	20.7	-19.25	446	2	0.033	0.017	0.97
152	160	230+005+010	423	2	301.6	907.5	32.8	-19.75	422	3	0.068	0.081	0.84
189	-	126+017+009	433	1	267.2	771.0	43.7	-19.70	409	4	0.066	0.195	0.35
198	82	152-000+009	473	1	284.7	863.9	38.7	-19.80	454	4	0.056	0.086	0.65
223	111	187+008+008	462	2	268.3	703.7	34.0	-19.60	442	3	0.054	0.139	0.39
228	133	203+059+007	643	4	210.6	644.0	31.1	-19.10	612	2	0.043	0.050	0.86
317	-	156+010+010	351	1	321.6	846.7	36.0	-20.00	345	5	0.077	0.226	0.34
332	106	175+005+009	333	1	291.0	664.3	27.3	-19.90	309	3	0.058	0.083	0.69
349	138	207+026+006	893	5	188.0	768.8	42.6	-19.15	703	5	0.056	0.119	0.47
351	138	207+028+007	615	4	225.4	689.1	33.0	-19.15	611	4	0.058	0.088	0.65
362	158	232+029+006	306	2	195.2	284.5	15.1	-18.80	305	2	-0.004	-0.004	1.00
366	158	217+020+010	353	0	300.4	763.4	31.1	-19.90	339	4	0.063	0.165	0.38
376	167	255+033+008	437	2	258.7	658.0	27.9	-19.50	415	3	0.058	0.029	1.03
474	76	133+029+008	389	3	251.2	612.6	43.3	-19.50	377	5	0.069	0.221	0.31
512	91	168+002+007	371	2	227.7	410.7	26.7	-19.40	321	3	0.036	0.091	0.39
525	109	177+055+005	438	4	154.2	312.6	19.3	-18.50	409	3	0.017	0.020	0.84
530	-	192+062+010	333	0	306.8	790.3	40.4	-20.00	316	5	0.077	0.223	0.34
548	143	216+016+005	314	2	158.7	227.1	14.6	-18.50	294	1	0.014	0.002	-
549	-	214+001+005	322	1	162.5	225.8	16.8	-18.60	308	1	0.015	0.027	-
550	154	227+007+004	459	3	135.1	287.5	18.2	-18.10	447	1	0.004	0.041	-
779	-	146+054+004	353	1	139.7	209.5	20.4	-18.00	353	2	0.013	0.014	0.94
796	93	167+026+003	369	1	102.3	161.7	11.9	-17.70	336	1	-0.003	0.001	-
827	-	189+003+008	405	0	254.1	572.4	30.0	-19.50	384	4	0.045	0.128	0.35

**Notes.** Columns in the table are as follows: (1)  $SCl_{ID}$ : the supercluster ID in the L10 catalogue; (2)  $ID_{E01}$ : the supercluster ID in the E01 catalogue; (3) the supercluster ID AAA+BBB+ZZZ, where AAA is RA, +/-BBB is Dec, and CCC is 100z; (4) the number of galaxies in the supercluster,  $N_{gal}$ ; (5) the number of groups with at least 30 member galaxies in the supercluster,  $N_{30}$ ; (6) the distance of the density maximum,  $d_{peak}$ ; (7) the total weighted luminosity of galaxies in the supercluster,  $L_{tot}$ ; (8) the supercluster diameter (the maximum distance between galaxies in the supercluster), Diam; (9) the absolute magnitude limit of the volume limited sample,  $R_{magV}$ ; (10) the number of galaxies in the volume limited sample,  $N_{galV}$ ; (11) the maximum value of the fourth Minkowski functional, ( $V_{3,max}$  (clumpiness), for the supercluster; (12)–(14): the shapefinders  $K_1$  (planarity) and  $K_2$  (filamentarity), and the ratio of the shapefinders  $K_1/K_2$  for the full supercluster (the ratio of the shapefinders is not determined for superclusters with  $V_{3,max} = 1$  for the full range of threshold densities, as explained in text).

interval for each supercluster and give the maximum value of  $V_3$  for each supercluster.

The first three Minkowski functionals have been used to calculate the dimensionless shapefinders  $K_1$  (planarity) and  $K_2$  (filamentarity) (Sahni et al. 1998; Shandarin et al. 2004; Saar 2009). The shapefinders are calculated in two steps. At first, specific combinations of Minkowski functionals are used to calculate the shapefinders, which describe the thickness, the width, and the length of a supercluster. With the thickness and the width we calculate the planarity  $K_1$  of a supercluster, and with the width and the length we calculate the filamentarity  $K_2$  of a supercluster. We give their formulae in Appendix B. Einasto et al. (2007d) showed that in the ( $K_1$ ,  $K_2$ ) shapefinder plane the morphology of superclusters is described by a characteristic curve (morphological signature). When the mass fraction increases, the changes in the morphological signature accompany the changes of the

fourth Minkowski functional. As the mass fraction increases, the planarity  $K_1$  almost does not change for a wide range of mass fractions (up to  $mf \approx 0.35$ ), while the filamentarity  $K_2$  increases – higher density regions of a supercluster are more filamentary than the whole supercluster. At higher mass fractions the planarity of superclusters starts to decrease. In rich superclusters studied previously (Einasto et al. 2007d) at a mass fraction of about  $mf = 0.7$ , the characteristic morphology of the supercluster changes rapidly. Both the planarity and filamentarity decrease – this is a crossover from the outskirts of the supercluster to the core of the supercluster. In high-density, clumpy cores of superclusters, where the isodensity surfaces have a complex shape, the planarity and filamentarity may even become negative (Sheth et al. 2003; Einasto et al. 2008). In Fig. 9 (Sect. 4.3) we plot the morphological signature with symbols of a size proportional to the value of the fourth Minkowski functional  $V_3$  at a given mass



**Table 2.** Abell clusters in superclusters.

(1)	(2)	(3)
$SCI_{ID}$	$ID_{E01}$	Abell ID
1	162	2142x, 2149x
10	160	2152
11	154	2040, 2028
24	111	1424, 1516
38	95	1173x, 1187
55	111	1358
60	160	2197
61	126, 136	1620, 1650x, 1658x, 1663x, 1692, 1750x, 1773x, 1780, 1809x
64	164	2223, 2244
87		1904
94	158	2067, 2065x, 2089
136	271	1569
152	160	2048, 2055x
198	82	933
223	111	1541, 1552
228	133	1767x
332	106	1346
336	109	1279, 1436
349	138	1795x, 1827, 1831x
350	160	2052x, 2063x
351	138	1775x, 1800x, 1831x
362	158	2073, 2079, 2092
376	167	2249x
474	76	699
512	91	1205x, 1238
525	109	1291x, 1377
548	143	1913
550	154	2028, 2055
796	93	1185x

**Notes.** Columns in the table are as follows: (1)  $SCI_{ID}$ : the supercluster ID in the L10 catalogue; (2)  $ID_{E01}$ : the supercluster ID in the E01 catalogue; (3) the Abell ID. x denotes X-ray clusters (E01, Böhringer et al. 2004).

Appendix C a 3D version of Fig. 3, and the 3D distributions of groups in superclusters with the right ascensions, declinations, and distances of groups.

In Fig. 3 the superclusters SCI 060 and SCI 350 (Table 1) are seen close to us. They belong to the Hercules supercluster, which is split into several superclusters in our sample. These are the nearby rich systems seen in Fig. 2. A chain of poor superclusters connects the Hercules supercluster with rich superclusters at a distance of about  $200 h^{-1}$  Mpc the superclusters SCI 349 and SCI 351 (the Bootes supercluster) among them. We mentioned in Sect. 2 that at small distances the size of the sample cross-section is only  $220 \times 140 h^{-1}$  Mpc and these superclusters may be broken up by the sample borders. Therefore the data on nearby superclusters are less reliable than the data on the more distant ones.

Rich superclusters at distances of about  $210\text{--}260 h^{-1}$  Mpc form three chains, separated by voids. A 3D figure on our web pages shows that actually only one of these supercluster systems is a clear chain-like system. This is the Sloan Great Wall (SGW), the richest galaxy system in the nearby Universe (Vogeley et al. 2004; Gott et al. 2005; Nichol et al. 2006; Einasto et al. 2010; Luparello et al. 2011; Pimblet et al. 2011; Einasto et al. 2011). The SGW consists of several superclusters of galaxies. The richest of them are the superclusters SCI 061 and SCI 024. The other two supercluster chains are much poorer and cannot really be called chains. One of them is separated from the SGW by a void;

the Bootes supercluster is the richest supercluster in this system. The richest supercluster in the third system of superclusters is the Ursa Majoris supercluster (SCI 336).

The very rich Corona Borealis supercluster is located at the joint of these systems. This supercluster is a member of a huge system of rich superclusters located at the right angle with respect to the Local Supercluster, described by Einasto et al. (1997b) as the dominant supercluster plane.

At high positive values of the  $x$  coordinate there are no rich clusters, and the superclusters in this region are also poor. There are some poor superclusters farther away, perhaps connecting superclusters in our sample volume with more distant superclusters. Thus the large-scale distribution of the superclusters is very inhomogeneous, as noted also in L10.

To make projection effects less significant, we do not show the chains of nearby superclusters in the right panel of Fig. 3. The superclusters SCI 548, SCI 549, SCI 550, SCI 350, and SCI 060 are superimposed on the superclusters SCI 351 and SCI 354, and the superclusters SCI 779 and SCI 796 on the superclusters SCI 038, SCI 336, and SCI 525.

#### 4.2. Morphology of superclusters

The results on the morphology of superclusters are summarised in Table 1 where we list the following morphological characteristics for each supercluster: the maximum value of the fourth Minkowski functional  $V_{3,max}$  (clumpiness), the values of the shapefinders  $K_1$  (planarity) and  $K_2$  (filamentarity) for the whole supercluster, and the ratio of the shapefinders  $K_1/K_2$  for the whole supercluster. This ratio is not given for the superclusters for which  $V_3 = 1$  over the whole mass fraction interval, because the  $K_2$  may become very small, making the ratio  $K_1/K_2$  noisy.

We began the analysis of the structure of superclusters by searching for possible subsets defined by their physical and morphological characteristics. For this purpose we applied the *Mclust* package for classification and clustering, described shortly in Sect. 3.2. Initial data for *Mclust* was the number of groups with at least 30 member galaxies, the total weighted luminosity of galaxies in a supercluster, its diameter, and the morphological parameters given in Table 1. The results of this analysis show that superclusters can be divided into two main sets. The first set consists of superclusters with shape parameter  $K_1/K_2 < 0.6$ , and second set of those with shape parameter  $K_1/K_2 > 0.6$  – these superclusters are less elongated than the superclusters in the first set. According to *Mclust*, the richest supercluster in our sample, the supercluster SCI 061, forms a separate subgroup owing to its very high luminosity. For simplicity, we include this supercluster in the following analysis in the set of more elongated superclusters.

We estimated how well superclusters are assigned to the two different sets using the uncertainty of classification calculated by *Mclust* (see Sect. 3.2). For our superclusters, the mean uncertainty of the classification is  $1.9 \times 10^{-2}$ , showing that superclusters are well classified. To measure how well the sets are determined and to find the best model of a given dataset we use the BIC values given by *Mclust*. For our sets of superclusters the lowest value of the BIC corresponds to the division of superclusters into two main sets, with SCI 061 forming a separate class. The value of the BIC for the one-component model for superclusters is higher, showing that this model is less likely for our superclusters.

Figure 4 presents the shapefinders  $K_1$  (planarity) and  $K_2$  (filamentarity) in the shapefinder's plane for our supercluster sample. In this figure circles correspond to those superclusters for

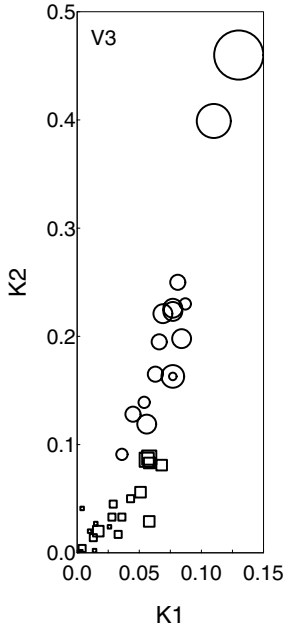
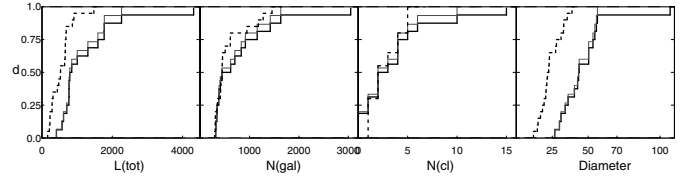


**Fig. 4.** Shapefinders  $K_1$  (planarity) and  $K_2$  (filamentarity) for the superclusters with their clumpiness. The symbol sizes are proportional to the fourth Minkowski functional  $V_{3,\max}$ . Circles denote superclusters with the shapefinders ratio  $K_1/K_2 < 0.6$  and squares denote the superclusters with the ratio  $K_1/K_2 \geq 0.6$ .

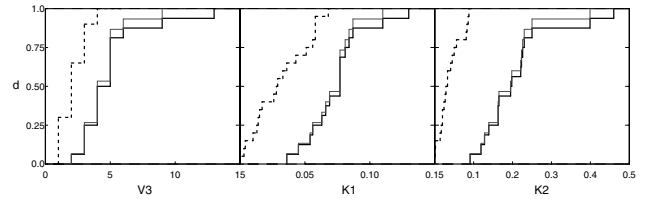
which the ratio of the shapefinders  $K_1/K_2 < 0.6$ , and squares to the superclusters with  $K_1/K_2 \geq 0.6$ , i.e. to more elongated and to less elongated superclusters, respectively. The symbol sizes are proportional to the maximum value of the fourth Minkowski functional  $V_{3,\max}$  (clumpiness). This figure reflects both the outer shape and the inner clumpiness (fine structure) of superclusters and summarises the morphological information about superclusters.

Table 1 and Fig. 4 demonstrate that almost all superclusters in our sample are elongated; they have large filamentarities with larger range of values than planarities. Two superclusters with the largest filamentarities and with the ratio of the shapefinders as small as  $K_1/K_2 = 0.28$  are the most extreme cases of filamentary systems in our sample. These two superclusters are the richest in our sample: SCI 061 and the Corona Borealis. We do not have extremely planar superclusters in our sample ( $K_1/K_2 \gg 1.0$ ). Three superclusters in our sample have  $K_1/K_2 \approx 1.0$  (they are spherical), and all these have a small maximum clumpiness ( $V_{3,\max} \leq 3$ ). More elongated superclusters typically have higher values of clumpiness  $V_3$  than less elongated ones – they have a more complicated morphology (see Table 3).

We present the median values of supercluster parameters in these sets in Table 3. In Fig. 5 we plot the cumulative distributions of the values of the physical characteristics of superclusters from the two sets, and in Fig. 6 the cumulative distributions of the morphological parameters. The scatter of the parameters is large, but the superclusters in the first set with the shape parameter  $K_1/K_2 < 0.6$  (with and without the supercluster SCI 061) are richer, more luminous, and have larger diameters than those in the second set with shape parameter  $K_1/K_2 \geq 0.6$ . Superclusters from the first set also have higher maximum values of the fourth Minkowski functional  $V_3$ , and higher values of planarities  $K_1$  and filamentarities  $K_2$ . In Fig. 7 we show another presentation of these results – the shapefinder’s plane for superclusters of different total luminosity and the richness (the number of galaxies in



**Fig. 5.** Cumulative distributions of the physical characteristics of superclusters for the two sets of superclusters divided by the value of the shape parameter. *From left to right:* the distributions of luminosities, numbers of galaxies, numbers of rich groups with at least 30 member galaxies, and diameters of superclusters. The black lines correspond to the first set of superclusters with  $K_1/K_2 < 0.6$ , including the supercluster SCI 061, the grey lines to the first set of superclusters without SCI 061, and the dashed lines to the second set of superclusters with  $K_1/K_2 > 0.6$ .



**Fig. 6.** Cumulative distributions of morphological parameters of superclusters for two sets of superclusters divided by the value of the shape parameter. *From left to right:* the distributions of the fourth Minkowski functional  $V_3$ , of planarities  $K_1$ , and filamentarities  $K_2$  of superclusters. The black lines correspond to the first set of superclusters with  $K_1/K_2 < 0.6$ , including the supercluster SCI 061, the grey lines to the first set of superclusters without SCI 061, and the dashed lines to the second set of superclusters with  $K_1/K_2 > 0.6$ .

**Table 3.** Parameters of superclusters in sets according to their morphology.

(1)	(2)		(3)	(4)
	$K_1/K_2 < 0.6$			$K_1/K_2 \geq 0.6$
	with SCI 061		without SCI 061	
$N_{\text{scl}}$	16		15	20
$Distance$	$254 \pm 64$		$254 \pm 66$	$200 \pm 43$
$L_{\text{tot}}$	$820 \pm 316$		$790 \pm 274$	$525 \pm 122$
$N_{\text{gal}}$	$530 \pm 207$		$442 \pm 176$	$445 \pm 129$
$N_{30}$	$2.5 \pm 0.92$		$2.0 \pm 0.74$	$2.0 \pm 0.63$
$Diameter$	$44 \pm 12$		$43 \pm 11$	$22 \pm 5$
$V_3$	$4.5 \pm 1.25$		$4.0 \pm 1.15$	$2.0 \pm 0.48$
$K_1$	$0.08 \pm 0.02$		$0.08 \pm 0.02$	$0.03 \pm 0.007$
$K_2$	$0.20 \pm 0.05$		$0.200 \pm 0.05$	$0.031 \pm 0.008$

**Notes.** Columns in the table are as follows: 1) the parameter:  $N_{\text{scl}}$ , the number of superclusters; the median distance of superclusters, in  $\text{Mpc}/h$ ; the median total weighted luminosity of galaxies in the superclusters,  $L_{\text{med}}$ , in  $10^{10} h^{-2} L_{\odot}$ ; the median number of galaxies in the superclusters,  $N_{\text{gal}}$ ; the median number of groups with at least 30 member galaxies in the superclusters,  $N_{30}$ ; the median diameter of the superclusters, in  $\text{Mpc}/h$ ; the median value of the fourth Minkowski functional,  $V_3$ ; the median values of the planarity  $K_1$  and filamentarity  $K_2$  of the superclusters; 2–3) the median values and  $1\sigma$  errors of the corresponding parameter for the first set of superclusters with the ratio of the shapefinders  $K_1/K_2 < 0.6$ ; 4) the median values and  $1\sigma$  errors of the corresponding parameter for the second set of superclusters with the ratio of the shapefinders  $K_1/K_2 \geq 0.6$ .

a supercluster) as coded in the symbol sizes explained in figure captions. The two most elongated superclusters are the richest and the most luminous.

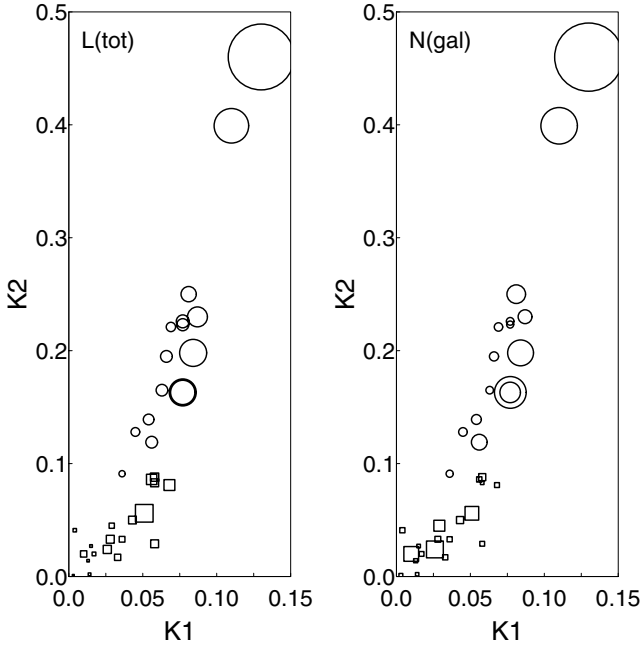


**Fig. 7.** Shapefinders  $K_1$  (planarity) and  $K_2$  (filamentarity), with the luminosities and richnesses of the superclusters. In the *left panel* symbol sizes are proportional to the total weighted luminosity of galaxies in the superclusters, and in the *right panel* to the number of galaxies in the superclusters. Circles and squares correspond to two sets of superclusters as in Fig. 4.

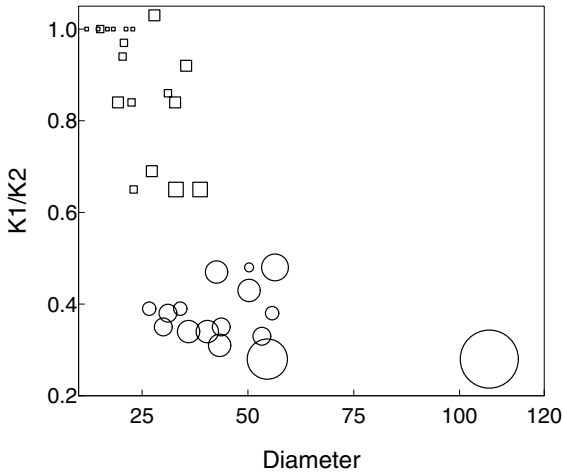


**Fig. 8.** Diameters of superclusters (in Mpc/h) vs. their shape parameter. Symbol sizes are proportional to the value of the fourth Minkowski functional  $V_3$  of a supercluster. Circles and squares correspond to the two sets of superclusters as in Fig. 4.

Figures 8 and 5 show that more elongated superclusters also have larger diameters than less elongated ones, implying that the systems with larger diameters are not planar structures. Also, there are no compact, planar, and very luminous superclusters.

Table 1 shows that all superclusters with the ratio of shapefinders with  $K_1/K_2 \geq 0.6$  are relatively nearby, only four of them lie at distances larger than  $250 h^{-1}$  Mpc. The closest of them is located at about  $90 h^{-1}$  Mpc, and their median distance is about  $200 h^{-1}$  Mpc. As mentioned above, owing to the sample geometry, the nearby superclusters may not be fully included in the sample volume and their small clumpiness may be due to this selection effect. Some nearby poor superclusters are located in low-density filaments between us and more distant

superclusters, and their shape and small clumpiness may be real (as noted also in Einasto et al. 1997b). The closest more elongated superclusters with the shape parameter  $K_1/K_2 < 0.6$  are about  $170 h^{-1}$  Mpc away from us, their mean and median distances almost coincide and are about  $254 h^{-1}$  Mpc (this is approximately the distance to the rich superclusters in the SGW).

#### 4.3. Notes on individual superclusters

Below, we give a short description of individual superclusters in our sample. In the figures of this section and in Appendix D we show for each supercluster (except for those for which  $V_3 = 1$  over the whole mass fraction interval) the sky distribution of supercluster members, the values of the fourth Minkowski functional  $V_3$  vs. the mass fraction  $mf$  and the morphological signature for each supercluster. Panels in these figures are as follows. The left panels show the sky distributions of galaxies in superclusters and the location of rich groups with at least 30 member galaxies. The middle panels show the clumpiness  $V_3$  vs. the mass fraction  $mf$  for a whole mass fraction interval from 0 to 1, and the right panels the shapefinder's ( $K_1, K_2$ ) curve (the morphological signature) for a supercluster. The mass fraction increases anti-clockwise along the curves. In these panels the value of mass fraction  $mf = 0.7$  is marked – at this value the morphological signature of rich superclusters changes. We will classify our superclusters as spiders, multispiders, filaments, and multi-branching filaments on the basis of their morphological information and visual appearance. Often superclusters are of intermediate type between these main types, hence for some superclusters our classification is a suggestion only.

We begin with the two richest superclusters from our sample (Fig. 9). For these two superclusters the morphological signature (Fig. 9, right panels) is plotted with symbols of the size proportional to the value of the fourth Minkowski functional  $V_3$  at a given mass fraction, to show how the morphological signature changes together with the changes in clumpiness, as described in Sect. 3.1. Here we do not mark the value of mass fraction  $mf = 0.7$ , for clarity.

*The supercluster SCI 061* at a distance of  $256 h^{-1}$  Mpc is the richest member of the SGW (Einasto et al. 2011; Luparello et al. 2011). This supercluster contains nine Abell clusters, the largest number in our sample. Five of these are also X-ray clusters (Böhlinger et al. 2004). The richest of them, A1750, is a merging X-ray cluster (Belsole et al. 2004). The morphology of SCI 061 resembles a multibranching filament with the maximum value of the fourth Minkowski functional  $V_{3,\max} = 13$ , and the ratio of the shapefinders  $K_1/K_2 = 0.28$ , one of the lowest in our catalogue (Fig. 9, upper row, and Table 1).

*The supercluster SCI 094* (the Corona Borealis supercluster) at a distance of  $215 h^{-1}$  Mpc is the second in richness among our sample. This system contains three Abell clusters (A2067, A2065, and A2089), and is a member of the dominant supercluster plane (Einasto et al. 1997b). The distribution of galaxies in the sky in SCI 094 is plotted in Fig. 9 (lower row, left panel). The maximum value of the fourth Minkowski functional of the Corona Borealis supercluster  $V_{3,\max} = 10$ , and the ratio of the shapefinders  $K_1/K_2 = 0.28$  (Fig. 9, the middle and right panels of the lower row, and Table 1). Morphologically SCI 094 is a multispiders with a number of clusters connected by low density filaments, with an overall very elongated shape that resembles a horse-shoe, with the merging X-ray cluster A2065 at the top (Chatzikos et al. 2006). SCI 094 has been studied by Small et al. (1998), who found that the core of this system probably has started to collapse. Numerical simulations show

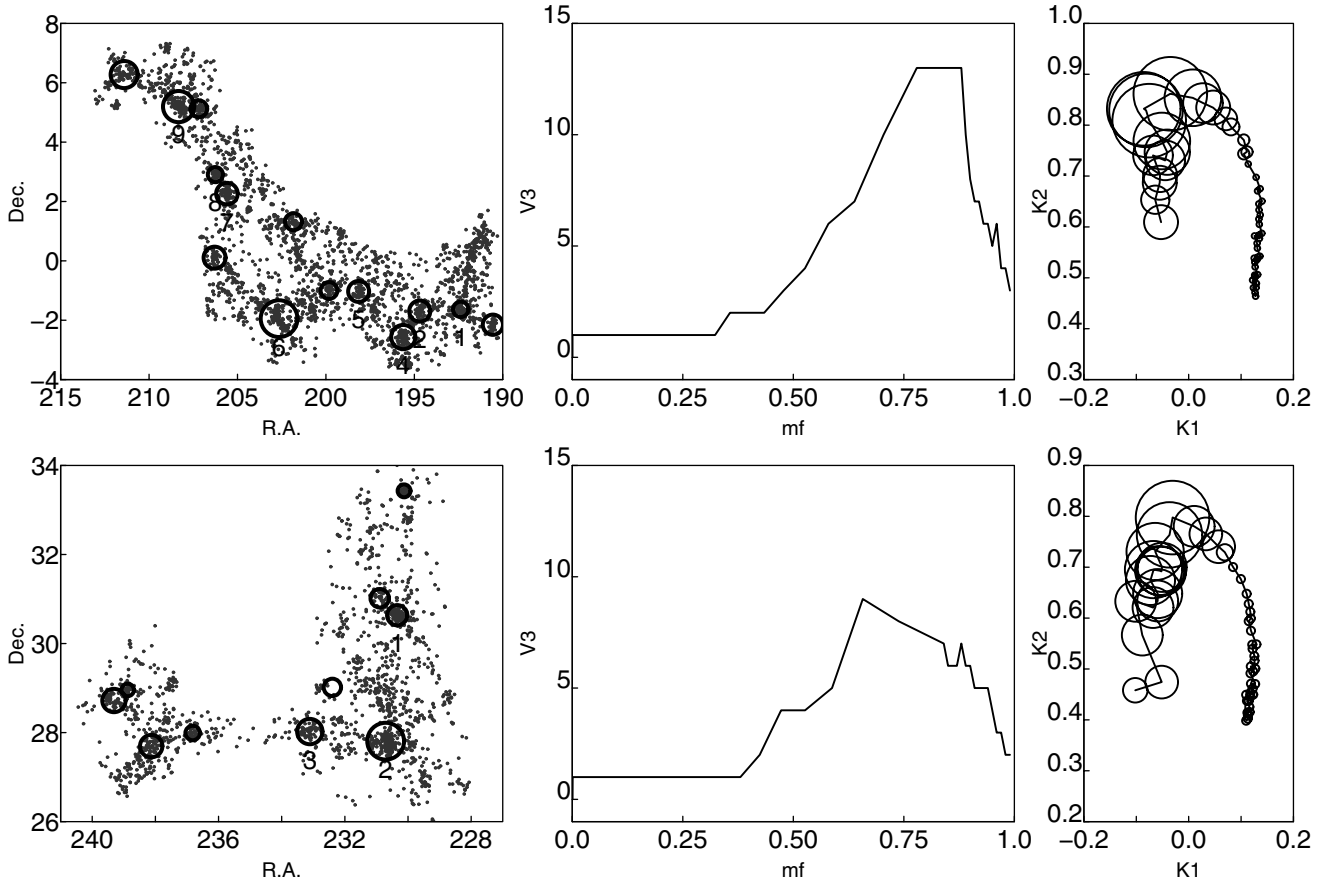


**Fig. 9.** *Left panels:* the distribution of galaxies (grey dots) in the sky, for the two superclusters, SCI 061 (*upper row*) and SCI 094 (*lower row*). Circles mark the location of groups with at least 30 member galaxies, and the size of a circle is proportional to the size of a group in the sky. The numbers show Abell clusters. The *middle panels* show the fourth Minkowski functional  $V_3$ , and the right panels the shapefinders  $K_1$  (planarity) and  $K_2$  (filamentarity) for a supercluster. The morphological signature in the  $K_1 - K_2$  plane is parametrically defined as  $K_1(mf)$  and  $K_2(mf)$ . The sizes of open circles are proportional to the value of  $V_3$  at a given mass fraction  $mf$ . They show the change of the clumpiness with the mass fraction together with the changes in the morphological signature. The Abell clusters in the supercluster SCI 061 (*upper row*) are 1 – A1620, 2 – A1650, 3 – A1658, 4 – 1663, 5 – 1682, 6 – 1750, 7 – 1773, 8 – 1780, and 9 – 1809. The Abell clusters in the supercluster SCI 094 (*lower row*) are 1 – A2067, 2 – A2065, and 3 – A2089.

that such collapsing cores in superclusters are rare (Gramann & Suhhonenko 2002). Luparello et al. (2011) proposed that SCI 094 may merge with several surrounding superclusters in the future. In last years interest in the Corona Borealis supercluster region has grown because of the discovery of the CMB cold spot in it's direction. This may be partly caused by the warm-hot diffuse gas in the supercluster filaments between the clusters, or by some undiscovered distant cluster (Génova-Santos et al. 2008; Padilla-Torres et al. 2009; Génova-Santos et al. 2010; Padilla-Torres et al. 2010, and references therein). The poor superclusters SCI 362 and SCI 366 are also members of the Corona Borealis supercluster. The morphology of SCI 362 resembles a simple spider with the ratio of the shapefinders  $K_1/K_2 = 1.0$ , while that of SCI 366 resembles a multibranching filament with the maximum value of the fourth Minkowski functional  $V_{3,\max} = 4$ , and the ratio of the shapefinders  $K_1/K_2 = 0.38$  (Fig. D.2).

The supercluster SCI 001 contains two rich Abell clusters, A2142 and A2149, both of them are X-ray sources (Table 2). Chandra observations have revealed that A2142 is probably still merging (Markevitch et al. 2000). SCI 001 is located in a region with a dense concentration of superclusters, close to SCI 011 and SCI 094. All these systems form a part of the dominant supercluster plane. At the location of SCI 001 the luminosity density

is the highest in the whole SDSS survey; this is probably at least partly because of the rich X-ray cluster A2142. The morphology of SCI 001 resembles a filament where clusters are located almost along a straight line (the 3D model on our web pages shows this best). The maximum value of the fourth Minkowski functional for SCI 001  $V_{3,\max} = 2$  and the ratio of the shapefinders  $K_1/K_2 = 0.48$  (Fig. 10 and Table 1).

The supercluster SCI 011 at a distance of  $234 h^{-1}$  Mpc contains two Abell clusters, A2040 and A2028, which are members of different superclusters in E01. The maximum value of the fourth Minkowski functional  $V_{3,\max} = 3$  (Fig. 10, middle row), the ratio of the shapefinders  $K_1/K_2 = 0.92$ . The morphology of SCI 011 resembles a sparse multispider or multibranching filament with a quite uniform density (as suggested by the low values of the fourth Minkowski functional  $V_3$  for a wide mass fraction interval). SCI 011 belongs to the same supercluster complex as SCI 001 (Fig. 3).

The supercluster SCI 024 at a distance of  $230 h^{-1}$  Mpc is the second richest member of the SGW. SCI 024 contains two Abell clusters, A1424 and A1516. Its morphology resembles a multispider with the maximum value of the fourth Minkowski functional  $V_{3,\max} = 5$  and the ratio of the shapefinders  $K_1/K_2 = 0.48$  (Fig. 10, lower row). The values of the fourth Minkowski functional of SCI 024 at small mass fractions ( $mf \approx 0.25$ )  $V_3 = 0$

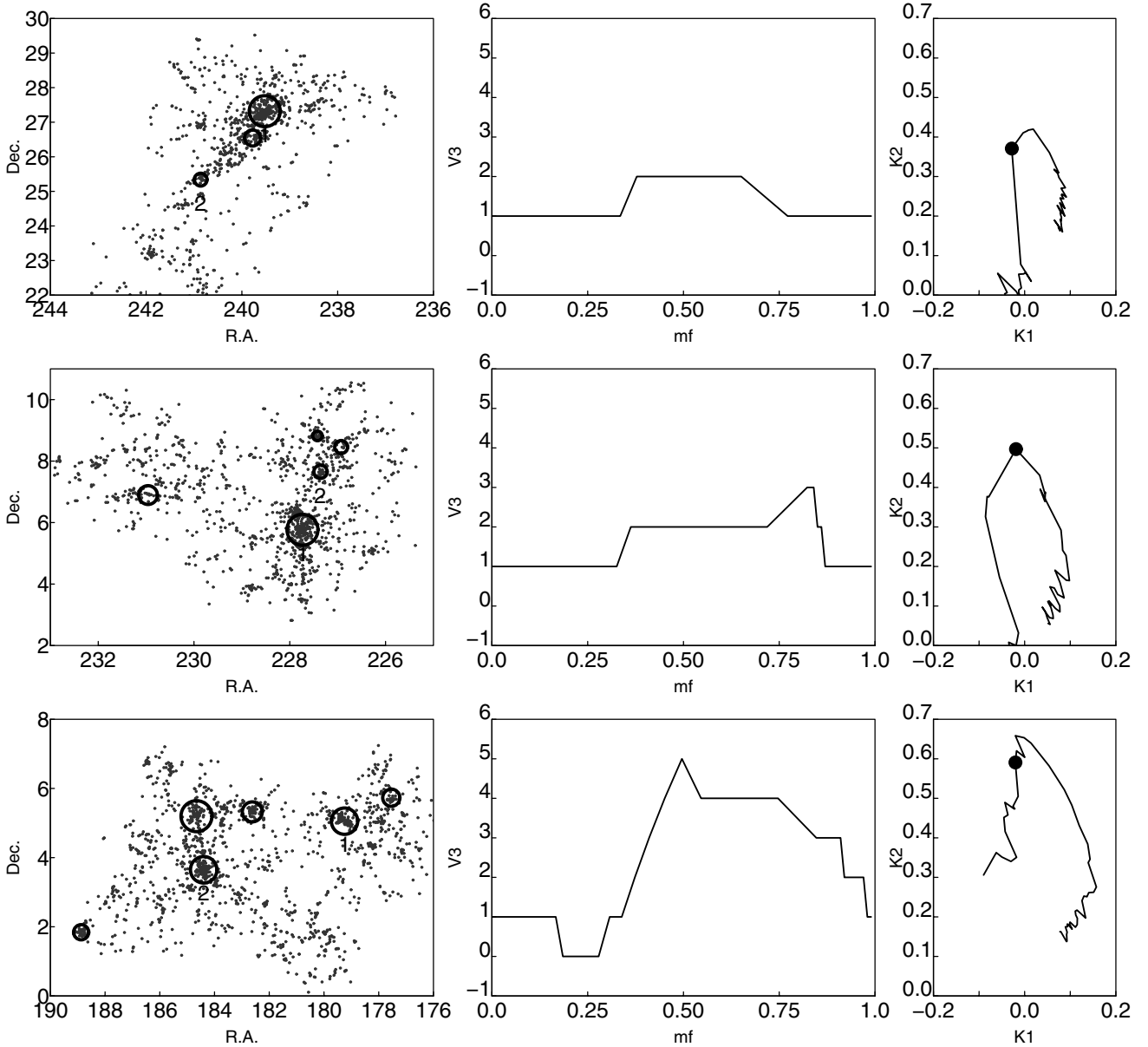


**Fig. 10.** Panels as in Fig. 9. Filled circles in the right panel mark the value of the mass fraction  $mf = 0.7$ . *Upper row:* the supercluster SCI 001. The Abell clusters are 1 – A2142 and 2 – A2149. *Middle row:* the supercluster SCI 011. The Abell clusters are 1 – A2040 and 2 – A2028. *Lower row:* the supercluster SCI 024. The Abell clusters are 1 – A1424 and 2 – A1516.

suggest that SCI 024 has low-density tunnels inside (Einasto et al. 2011). The member of the supercluster SCI 111 in E01 to which SCI 024 also belong, the poor supercluster SCI 223, can be described as a multispider with two concentrations – the fourth Minkowski functional has a value of 2 for a wide mass fraction interval (Fig. D.1). SCI 223 is separated from SCI 024 and SCI 055 by a small void, showing that clusters gathered together into one supercluster in the E01 catalogue sometimes do not belong to the same supercluster, when systems are determined using data on galaxies.

The supercluster SCI 055 at a distance of  $242 h^{-1}$  Mpc is separated from the SGW by a void and is connected to it by a filament of galaxies (this is the reason why SCI 024 and SCI 055 both belong to the supercluster SCI 111 in the E01 catalogue). SCI 055 contains one Abell cluster, A1358. The morphology of SCI 055 resembles a multibranching filament or an elongated multispider with the maximum value of the fourth Minkowski

functional  $V_{3,\max} = 5$  and the ratio of the shapefinders  $K_1/K_2 = 0.43$  (Fig. 11).

The supercluster SCI 336 contains two Abell clusters, A1279 and A1436, which are members of the Ursa Majoris supercluster (Fig. 11, middle row). SCI 336 belongs to a chain of superclusters that is separated by a void from SCI 349 and SCI 351 (the Bootes supercluster) (see also Kopylova & Kopylov 2009, and references therein). Luparello et al. (2011) found that several filamentary systems may be associated with this system. According to our calculations, the morphology of the Ursa Majoris supercluster resembles a sparse multibranching filament with the maximum value of the fourth Minkowski functional  $V_{3,\max} = 4$ , and the ratio of the shapefinders  $K_1/K_2 = 0.33$  (Fig. 11). The poor supercluster SCI 525 is also a member of the Ursa Majoris supercluster, morphologically SCI 525 can be described as a spider.

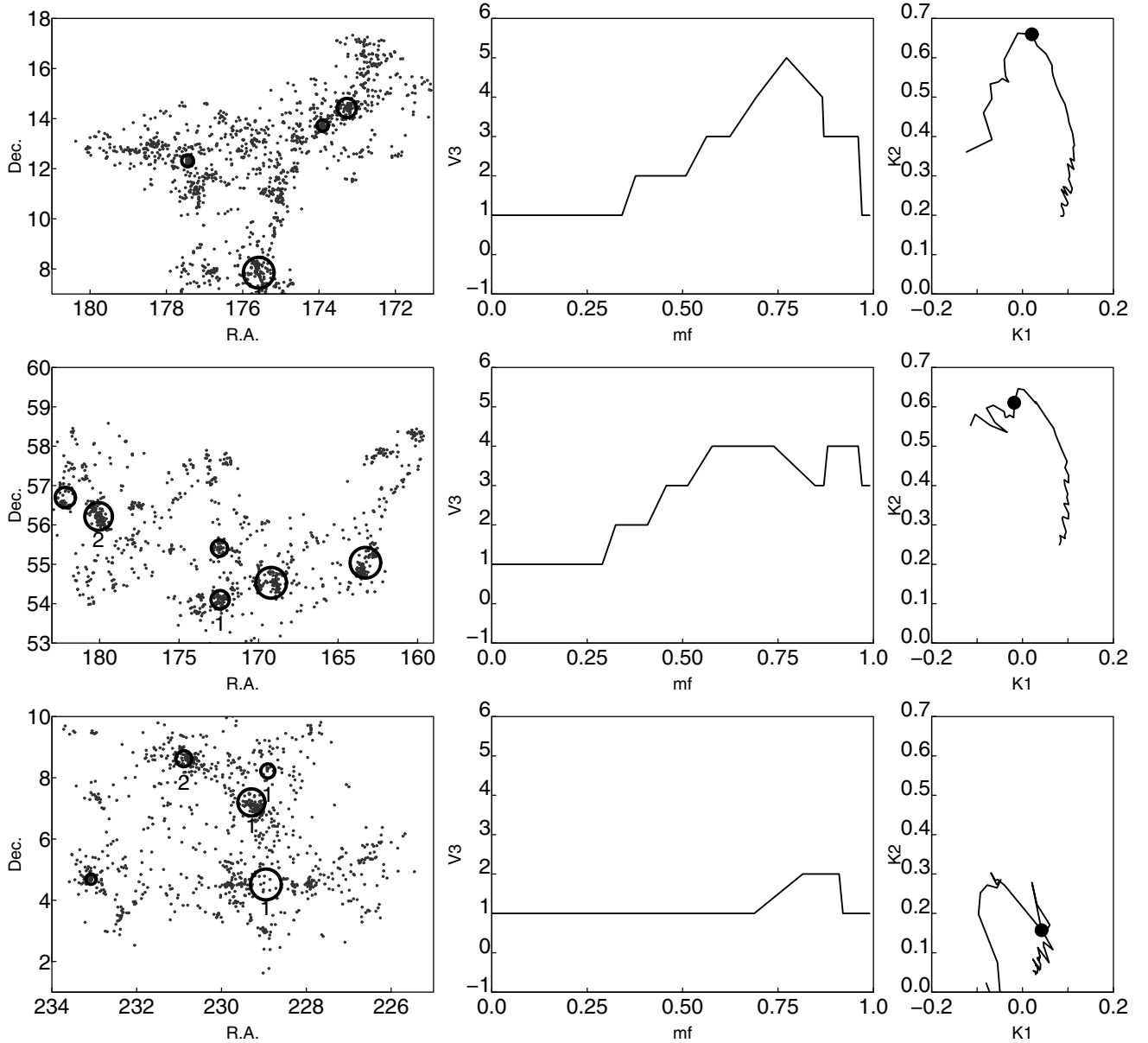


**Fig. 11.** Panels are the same as in Fig. 9. *Upper row:* the supercluster SCI 055. The Abell cluster is A1358. *Middle row:* the supercluster SCI 336. The Abell clusters are 1 – A1279, 2 – A1436. *Lower row:* the supercluster SCI 350. The Abell clusters are 1 – A2052, 2 – A2063.

The superclusters SCI 010, SCI 060, and SCI 350 belong to the rich Hercules supercluster that is split between several systems in our present catalogue. They are located at a distance of about  $100 h^{-1}$  Mpc and contain clusters that are exceptionally rich in the T10 catalogue, owing to their small distance from us (A2152 in SCI 010 and A2197 in SCI 060). This is the reason why the value of the fourth Minkowski functional for SCI 010 and SCI 060  $V_3 = 1$  over the whole mass fraction interval, showing that they contain only one high density clump. SCI 350 contains five rich clusters, three of them correspond to the Abell cluster A2052. This suggests that A2052 has a substructure, with different components corresponding to different groups and clusters in the T10 catalogue. The maximum value of the fourth Minkowski functional for SCI 350,  $V_{3,\max} = 2$  (Fig. 11, lower row), and the ratio of the shapefinders  $K_1/K_2 = 0.65$ . At the farther end SCI 350 chain joins the dominant supercluster plane (Fig. 3).

We summarise the results of the morphological analysis of the superclusters in Table 4. For clarity we present the figures

of the distribution of galaxies and rich groups/clusters in the sky for superclusters with less than 950 members galaxies, as well as their fourth Minkowski functionals and the morphological signatures in Appendix D.

In Table 4 we list for every supercluster their distance, the numbers of galaxies, the number of rich groups with at least 30 member galaxies, and the number of Abell clusters among them. From morphological parameters we list the maximum value of the fourth Minkowski functional and the number that shows whether the supercluster belongs to the set 1 (more elongated superclusters) or to the set 2 (less elongated superclusters). We also give morphological descriptions of superclusters and notes.

Table 4 shows that superclusters with a smaller number of galaxies also contain, as expected, a smaller number of rich groups and Abell clusters. Among them less elongated superclusters dominate over more elongated superclusters – there are 16 systems from set 2 and 10 from set 1 among them. The morphology of 14 of them can be described as simple spider

**Table 4.** Data of the morphology of superclusters.

(1) $SCl_{ID}$	(2) $d_{peak}$ Mpc/h	(3) $N_{gal}$	(4) $N_{30}$	(5) $N_{Abell}$	(6) $V_{3,max}$	(7) Set	(8) <i>Morph.</i>	(9) Notes
1	264.5	1038	4	2	2	1	F	
10	111.9	1463	2	1	1	2	S	
11	235.0	1222	5	2	3	2	mS(mF)	
24	230.4	1469	4	2	6	1	mS	SGW
55	242.0	1306	4	1	5	1	mS(mF)	
60	92.0	1335	3	1	1	2	S	
61	255.6	3056	15	9	13	1	mF	SGW
94	215.4	1830	10	3	9	1	mS	
336	170.0	1005	6	2	4	1	mF	
350	105.8	955	5	2	2	2	mS	
38	224.4	586	5	2	2	2	S	
64	301.7	619	2	2	3	1	F	
87	213.4	445	1	1	2	2	S	
136	212.1	504	5	1	2	2	S	
152	301.6	423	2	2	3	2	F	
189	267.2	433	1	0	4	1	F	
198	284.7	473	1	1	4	2	mF	
223	268.3	462	2	2	3	1	mS	
228	210.6	643	4	1	2	2	F	
317	321.6	351	1	0	5	1	mS	T
332	291.0	333	1	1	3	2	mS	
349	188.0	893	5	3	5	1	mS	F(L11)
351	225.4	615	4	3	4	2	mF	
362	195.2	306	2	3	2	2	mS	
366	300.4	353	0	0	4	1	mF	
376	258.7	437	2	1	3	2	F	T
474	251.2	389	3	1	5	1	F	
512	227.7	371	2	2	3	1	mF	
525	154.2	438	4	2	3	2	mS	
530	306.8	333	0	0	5	1	mS	T
548	158.7	314	2	1	1	2	S	Her-DSP
549	162.5	322	1	0	1	2	S	Her-DSP
550	135.1	459	3	2	1	2	S	Her-DSP
779	139.7	353	1	0	2	2	mS	SGW chain
796	102.3	369	1	1	1	2	S	SGW chain
827	254.1	405	0	0	4	1	F	

**Notes.** Columns in the table are as follows: (1)  $SCl_{ID}$ : the supercluster ID in the L10 catalogue; (2) the distance of the density maximum,  $d_{peak}$ ; (3) the number of galaxies in the supercluster,  $N_{gal}$ ; (4) the number of groups with at least 30 member galaxies in the supercluster,  $N_{30}$ ; (5) the number of Abell clusters among groups with at least 30 member galaxies in the supercluster,  $N_{Abell}$ ; (6) the maximum value of the fourth Minkowski functional, ( $V_{3,max}$  (clumpiness), for the supercluster; (7) classification: set – 1 for superclusters with the ratio of the shapefinders  $K_1/K_2 < 0.6$  and 2 for superclusters with the ratio of the shapefinders  $K_1/K_2 \geq 0.6$ ); (8) morphology: S denotes spiders, mS – multispiders, F – filaments and mF – multibranching filaments; (9) notes. SGW denotes members of the Sloan Great Wall; F(L11) denotes a filamentary system according to (Luparello et al. 2011); T denotes superclusters for which at a certain mass fraction  $V_3 = 0$ , suggesting that these superclusters have tunnels through them (Appendix B, Einasto et al. 2011). Her-DSP denotes the superclusters located in a chain of superclusters that connects the Hercules supercluster with the dominant supercluster plane, and SGW chain denotes the superclusters in a chain in the foreground of the Sloan Great Wall.

or simple filament, and 12 of them are either multispiders or multibranching filaments. In contrast, of 10 superclusters with at least 950 member galaxies 7 can be described as multispiders of multibranching filaments, two of them are simple spiders and one is a simple filament.

## 5. Discussion

### 5.1. Selection effects

The main selection effect in our study comes from the use of the flux-limited sample of galaxies to determine the luminosity density field and superclusters. To keep the luminosity-dependent selection effects as small as possible, we used data on galaxies and galaxy systems for a distance interval 90–320  $h^{-1}$  Mpc. In this interval these effects are the smallest (we refer to T10 for details). We calculate Minkowski functionals of individual superclusters from volume limited samples. This approach makes

the calculations of morphology insensitive to luminosity dependent selection effects.

Another selection effect comes from the choice of the density level used to determine superclusters. At the density level applied in the present paper ( $D = 5.0$ ), rich superclusters do not percolate yet. For example, in the SGW we see several individual rich superclusters. At a lower threshold density these superclusters join into a huge system. In the same time the Corona Borealis supercluster is split into several superclusters in our catalogue at the density level  $D = 5.0$ . Thus there is no unique density level, which would be the best choice for all superclusters. However, L10 show that superclusters are fairly well-defined systems and do not change much when changing the density level, if only this change is small and does not break them up into small systems or does not join them into huge percolating systems. When we move towards higher density levels,

some galaxies and galaxy systems in the lower density outskirts of a supercluster do not belong to the supercluster any more; in that case the clumpiness of the supercluster at low mass fractions may decrease. Moving towards lower density levels, new galaxies and galaxy systems in the outskirts of a supercluster become supercluster members. This may increase the value of the clumpiness and change the morphological signature of a supercluster at low mass fractions. The possible change in morphology depends on the number of galaxies and on the richness of groups removed from or added to the supercluster and is individual for each supercluster.

At small distances our sample volume is small, which introduces another selection effect – nearby rich superclusters are split between several superclusters, some parts of these superclusters may be located outside of the sample volume. This makes the data about nearby superclusters less reliable.

The identification of Abell clusters may also be affected by selection effects. It is well known that some Abell clusters consist of several line-of-sight components. A good example of such a cluster is the cluster Abell 1386, recently studied by Pimblet et al. (2011). Our search discarded Abell clusters affected by this projection effect.

## 5.2. Comparison with other studies

Recently Costa-Duarte et al. (2011) used volume-limited samples of galaxies from the SDSS DR7 to extract superclusters of galaxies and to study the morphology of whole superclusters with the shape parameter (the ratio of the shapefinders  $K_1/K_2$ ). To determine superclusters the authors calculated the density field with an Epanechnikov kernel and found systems of galaxies with at least 10 member galaxies. In Einasto et al. (2007d), we compared the Epanechnikov and  $B_3$  box spline kernels and found that both kernels are good to describe the overall shape of superclusters, while the  $B_3$  box spline kernel better resolves the inner structure of superclusters. This is the reason why we used this kernel in the present study. The most important difference between our studies is that we used the data about the richer superclusters with at least 300 member galaxies. Costa-Duarte et al. (2011) showed that there are both planar and filament-like superclusters (pancakes and filaments) among the superclusters of their sample, while in our sample there are almost no superclusters for which planarity is larger than filamentarity. However, Costa-Duarte et al. (2011) found that very rich and luminous superclusters tend to be filaments, as we also found in our study.

The overall shapes of superclusters, described by the shape parameters or approximated by triaxial ellipses, have been analysed in Jaaniste et al. (1998); Kolokotronis et al. (2002); Basilakos (2003); Einasto et al. (2007a); Costa-Duarte et al. (2011); Luparello et al. (2011). These studies showed that elongated, prolate structures dominate among superclusters, as we also found in our study. In the analysis of the geometry of the structures around the galaxy clusters from simulations Noh & Cohn (2011) showed that these structures tend to lie on planes. Similarly, in our study and in the study by Costa-Duarte et al. (2011) poorer systems are more planar. Sheth et al. (2003) used the shapefinders plane  $K_1-K_2$  (the morphological signature in our study) to study the morphology of superclusters in simulations. They found that richer and more massive superclusters tend to be more filamentary and have a more complicated inner structure (high values of the genus in their study).

Future evolution of the structure in the Universe has been addressed in simulations by several authors, we refer to Araya-Melo et al. (2009) for a review and references.

Araya-Melo et al. (2009) studied the evolution of the shape and inner structure of superclusters in simulations from the present time to a distant future (from  $a = 1$  to  $a = 100$ ,  $a$  is the expansion factor). In their study superclusters were defined as high-mass bound objects, and the supercluster shape was approximated by triaxial ellipses. To analyse the substructure of superclusters they used the multiplicity function of clusters in superclusters. Araya-Melo et al. (2009) showed that superclusters are elongated, prolate structures, there are no thin pancakes among them. Future superclusters are typically much more spherical than present-day superclusters. Presently, the superclusters contain a large number of clusters, which may merge into a single cluster in the far future, i.e., multispiders and multibranching filaments may evolve into simple spiders and filaments.

Comparisons of the properties of rich and poor superclusters have revealed several differences between them. The mean and maximum number densities of galaxies in rich superclusters are higher than in poor superclusters. Rich superclusters are more asymmetrical than poor superclusters (Einasto et al. 2007a). Rich superclusters contain high-density cores (Einasto et al. 2007c). The fraction of rich clusters and X-ray clusters in rich superclusters is larger than in poor superclusters (Einasto et al. 2001; Luparello et al. 2011), and the core regions of the richest superclusters may contain merging X-ray clusters (Bardelli et al. 2000; Rose et al. 2002). However, we still lack a detailed analysis of whether the differences between the properties of the galaxy and group content of rich and poor superclusters are related also to the differences in morphology of superclusters.

In Einasto et al. (2008) we compared the properties of the two richest superclusters from the 2dF Galaxy Redshift Survey, the superclusters SCI 126 (SCI 061 in the present study), and the Sculptor supercluster (SCI 9 in E01). We used Minkowski functionals to quantify the fine structure of these superclusters as traced by different galaxy populations. Our calculations showed that in the supercluster SCI 126 the population of red, early type galaxies is more clumpy than the population of blue, late type galaxies, especially in the outskirts of the supercluster. In contrast, in the supercluster SCI 9 the clumpiness of galaxies of different type is quite similar in its outskirts. In the core of the supercluster SCI 9 the clumpiness of blue, late type galaxies is larger than the clumpiness of red, early type galaxies. In the supercluster SCI 111 in the SGW the clumpiness of red galaxies is larger than that of blue galaxies (Einasto et al. 2011). Morphologically the supercluster SCI 126 resembles a multibranching filament, while the Sculptor supercluster and SCI 111 resemble a multispider. We need to study the morphology and galaxy populations of a larger sample of superclusters to find out whether the differences between galaxy populations in superclusters are also related to their different morphology.

Aragón-Calvo et al. (2010) recently studied the structure and morphologies of elements that define the cosmic web with the Multiscale Morphology Filter and data from  $\Lambda$ CDM simulations. The authors found several typical morphologies for filaments, which they describe as line, grid, star, and complex filaments. We can compare that with our classification of supercluster morphologies. Approximately, line filaments are comparable with our simple filaments. Star filaments can be compared with simple spiders. Grid and complex filaments may correspond either to multibranching filaments or to multispiders, although complex filaments are more similar to multispiders and grid filaments to multibranching filaments. This shows that the morphology of observed and simulated superclusters is, in general, similar, as we found earlier from much smaller samples

of observed and simulated superclusters. The biggest exception is the supercluster SCI 061, a very rich and high-density multi-branching filament. No other supercluster with such a morphology has been found yet either in simulations or observations (see also [Gott et al. 2008](#)). Another difference between the observed and simulated superclusters, as quantified by Minkowski functionals and shapefinders, is the fine structure of superclusters, delineated by galaxies of different luminosity ([Einasto et al. 2007d](#)). The clumpiness of observed superclusters for galaxies of different luminosity has a much larger scatter than that of simulated superclusters. Simulations do not yet explain all the features of observed superclusters.

## 6. Summary and conclusions

We have presented an analysis of the large-scale distribution and morphology of superclusters from the SDSS DR7. While the overall shape of superclusters has been analysed earlier in several studies, our paper is the first in which the inner morphology of a large sample of observed superclusters is studied in detail. We used multidimensional normal mixture modelling to divide superclusters into two sets according to their physical and morphological properties. We present 2D and 3D distributions of galaxies and rich groups in superclusters, the clumpiness curve (the fourth Minkowski functional  $V_3 - mf$  relation), as well as the morphological signature  $K_1 - K_2$  for each supercluster in our sample.

The superclusters were selected to contain at least 300 observed galaxies. As we showed, this does not mean that all superclusters in our sample are rich – about 1/4 of our superclusters contain one rich cluster or group only (three superclusters do not contain any rich group or cluster).

Summarising, our study showed that:

- 1) Most superclusters contain Abell clusters, about 1/3 of them are X-ray clusters.
- 2) The large-scale distribution of the superclusters is very inhomogeneous. Rich superclusters in the sample form three chains, the Sloan Great Wall is the richest of them.
- 3) Almost all superclusters under study are elongated and have filamentarities that are larger than their planarities. More elongated superclusters are also more luminous, have larger diameters and contain a larger number of rich clusters. The values of the fourth Minkowski functional  $V_3$  show that they also have a more complicated inner morphology than less elongated superclusters.
- 4) The morphological analysis shows a large variety of morphologies among superclusters. The fine structure of superclusters can be described with four main types of morphology: spiders, multispiders, filaments, and multi-branching filaments. Often a supercluster has an intermediate morphology between these main types. Superclusters with a similar shape parameter may have a different fine structure. Consequently neither the shape parameter or the number of rich clusters in a supercluster alone are sufficient to describe the morphology of superclusters.

Our results on the morphology of superclusters can be used to compare the properties of local and high-redshift superclusters. Few superclusters at very high redshifts have already been discovered in deep, wide-field imaging surveys ([Nakata et al. 2005](#); [Swinbank et al. 2007](#); [Gal et al. 2008](#); [Tanaka et al. 2009](#); [Schirmer et al. 2011](#)). Deep surveys like the ALHAMBRA

project ([Moles et al. 2008](#)) will provide us with data about (possible) very distant superclusters; we can analyse their structure and compare that with the local superclusters, using morphological methods.

Our study does not give a definite answer to the question about the possible connection between the morphology of superclusters and their large-scale distribution. Also, there are superclusters in our sample that can be described as filaments or multi-branching filaments, but none of them is as rich and has such an overall high density as the supercluster SCI 061. Even the richest supercluster with a multispider morphology in our sample, the supercluster SCI 094, is not as rich as the very rich Sculptor supercluster in [Einasto et al. \(2007d\)](#). This shows the need for a larger sample of superclusters to understand the morphological variety of superclusters, and to study the possible connection between the large-scale distribution of superclusters and their morphology.

Different morphologies of superclusters suggest that their evolution has been different. To understand the formation and evolution of superclusters of different morphology better, we need to study the properties and evolution of superclusters in simulations. The morphology of superclusters and its evolution may be one of the factors to distinguish between different cosmological models ([Kolokotronis et al. 2002](#); [Hoffman et al. 2007](#)). Especially interesting is the supercluster SCI 061 in the Sloan Great Wall. Up to now simulations have not been able to model its morphology ([Einasto et al. 2007d](#), and references therein). New simulations with larger volumes are needed to study the morphology of superclusters and the evolution of the morphology of simulated superclusters, to understand the reasons for the exceptional morphology of the supercluster SCI 061. In addition, very rich superclusters are rare; another reason to use simulations for large volumes comes from the demand to include as large a variety of superclusters in the simulation volume as possible.

*Acknowledgements.* We thank our referee for a very detailed review with many useful suggestions that helped to improve the paper.

Funding for the Sloan Digital Sky Survey (SDSS) and SDSS-II has been provided by the National Science Foundation, the US Department of Energy, the National Aeronautics and Space Administration, the Japanese Monbukagakusho, and the Max Planck Society, and the Higher Education Funding Council for England. The SDSS Web site is <http://www.sdss.org/>.

The SDSS is managed by the Astrophysical Research Consortium (ARC) for the Participating Institutions. The Participating Institutions are the American Museum of Natural History, Astrophysical Institute Potsdam, University of Basel, University of Cambridge, Case Western Reserve University, The University of Chicago, Drexel University, Fermilab, the Institute for Advanced Study, the Japan Participation Group, The Johns Hopkins University, the Joint Institute for Nuclear Astrophysics, the Kavli Institute for Particle Astrophysics and Cosmology, the Korean Scientist Group, the Chinese Academy of Sciences (LAMOST), Los Alamos National Laboratory, the Max-Planck-Institute for Astronomy (MPIA), the Max-Planck-Institute for Astrophysics (MPA), New Mexico State University, Ohio State University, University of Pittsburgh, University of Portsmouth, Princeton University, the United States Naval Observatory, and the University of Washington.

We acknowledge the Estonian Science Foundation for support under grants Nos. 8005 and 7146, and the Estonian Ministry for Education and Science support by grant SF0060067s08. This work has also been supported by the University of Valencia through a visiting professorship for Enn Saar and by the Spanish MEC project AYA2006-14056, “PAU” (CSD2007-00060), including FEDER contributions, the Generalitat Valenciana project of excellence PROMETEO/2009/064, and by Finnish Academy funding. J.E. thanks Astrophysikalisches Institut Potsdam (using DFG-grant Mu 1020/15-1), where part of this study was performed. The density maps and the supercluster catalogues were calculated at the High Performance Computing Centre, University of Tartu. In this paper we use  $R$ , an open-source free statistical environment developed under the GNU GPL ([Ihaka & Gentleman 1996](#), <http://www.r-project.org>).

## Appendix A: Luminosity density field and superclusters

To calculate the luminosity density field, we must first calculate the luminosities of groups. In flux-limited samples galaxies outside the observational window remain unobserved, and we have also to take into account the luminosities of these galaxies as well. For that, we multiply the observed galaxy luminosities by the luminosity weight  $W_d$ . The distance-dependent weight factor  $W_d$  was calculated as follows:

$$W_d = \frac{\int_0^\infty L n(L) dL}{\int_{L_1}^{L_2} L n(L) dL}, \quad (\text{A.1})$$

where  $L_{1,2} = L_\odot 10^{0.4(M_\odot - M_{1,2})}$  are the luminosity limits of the observational window at a distance  $d$ , corresponding to the absolute magnitude limits of the survey  $M_1$  and  $M_2$ ; we took  $M_\odot = 4.64$  mag in the  $r$ -band (Blanton & Roweis 2007). Owing to their peculiar velocities, the distances of galaxies are somewhat uncertain; if the galaxy belongs to a group, we used the group distance to determine the weight factor.

To calculate a luminosity density field, we converted the spatial positions of galaxies  $\mathbf{r}_i$  and their luminosities  $L_i$  into spatial (luminosity) densities. For that we use kernel densities (Silverman 1986):

$$\rho(\mathbf{r}) = \sum_i K(\mathbf{r} - \mathbf{r}_i; a) L_i, \quad (\text{A.2})$$

where the sum is over all galaxies, and  $K(\mathbf{r}; a)$  is a kernel function of a width  $a$ . Good kernels for calculating densities on a spatial grid are generated by box splines  $B_J$ . Box splines are local and they are interpolating on a grid:

$$\sum_i B_J(x - i) = 1, \quad (\text{A.3})$$

for any  $x$  and a small number of indices that give non-zero values for  $B_J(x)$ . We used the popular  $B_3$  spline function:

$$B_3(x) = \frac{1}{12} (|x - 2|^3 - 4|x - 1|^3 + 6|x|^3 - 4|x + 1|^3 + |x + 2|^3). \quad (\text{A.4})$$

We defined the (one-dimensional)  $B_3$  box spline kernel  $K_B^{(1)}$  of the width  $a$  as

$$K_B^{(1)}(x; a, \delta) = B_3(x/a)(\delta/a), \quad (\text{A.5})$$

where  $\delta$  is the grid step. This kernel differs from zero only in the interval  $x \in [-2a, 2a]$ ; it is close to a Gaussian with  $\sigma = 1$  in the region  $x \in [-a, a]$ , so its effective width is  $2a$  (see, e.g., Saar 2009). The kernel exactly preserves the interpolation property for all values of  $a$  and  $\delta$ , where the ratio of  $a/\delta$  is an integer. (This kernel can be used also if this ratio is not an integer, and  $a \gg \delta$ ; the kernel sums to 1 in this case, too, with a very small error). This means that if we apply this kernel to  $N$  points on a one-dimensional grid, the sum of the densities over the grid is exactly  $N$ .

The three-dimensional kernel  $K_B^{(3)}$  is given by the direct product of three one-dimensional kernels:

$$K_B^{(3)}(\mathbf{r}; a, \delta) \equiv K_3^{(1)}(x; a, \delta) K_3^{(1)}(y; a, \delta) K_3^{(1)}(z; a, \delta), \quad (\text{A.6})$$

where  $\mathbf{r} \equiv \{x, y, z\}$ . Although this is a direct product, it is isotropic to a good degree (Saar 2009).

The densities were calculated on a Cartesian grid based on the SDSS  $\eta, \lambda$  coordinate system, because it allowed the most efficient fit of the galaxy sample cone into a brick. Using the rms velocity  $\sigma_v$ , translated into distance, and the rms projected radius  $\sigma_r$  from the group catalogue (T10), we suppressed the cluster finger redshift distortions. We divided the radial distances between the group galaxies and the group centre by the ratio of the rms sizes of the group finger:

$$d_{\text{gal},f} = d_{\text{group}} + (d_{\text{gal},i} - d_{\text{group}}) \sigma_r / \sigma_v. \quad (\text{A.7})$$

This removes the smudging effect the fingers have on the density field. We used an  $1 h^{-1}$  Mpc step grid and chose the kernel width  $a = 8 h^{-1}$  Mpc. This kernel differs from zero within the radius  $16 h^{-1}$  Mpc, but significantly so only inside the  $8 h^{-1}$  Mpc radius.

Before extracting superclusters we applied the DR7 mask constructed by Arnalte-Mur (Martínez et al. 2009; Liivamägi et al. 2010) to the density field and converted densities into units of mean density. The mean density is defined as the average over all pixel values inside the mask. The mask is designed to follow the edges of the survey and the galaxy distribution inside the mask is assumed to be homogeneous.

## Appendix B: Minkowski functionals and shapefinders

For a given surface the four Minkowski functionals (from the first to the fourth) are proportional to the enclosed volume  $V$ , the area of the surface  $S$ , the integrated mean curvature  $C$ , and the integrated Gaussian curvature  $\chi$ . Consider an excursion set  $F_{\phi_0}$  of a field  $\phi(\mathbf{x})$  (the set of all points where the density is higher than a given limit,  $\phi(\mathbf{x} \geq \phi_0)$ ). Then, the first Minkowski functional (the volume functional) is the volume of this region (the excursion set):

$$V_0(\phi_0) = \int_{F_{\phi_0}} d^3x. \quad (\text{B.1})$$

The second Minkowski functional is proportional to the surface area of the boundary  $\delta F_{\phi_0}$  of the excursion set:

$$V_1(\phi_0) = \frac{1}{6} \int_{\delta F_{\phi_0}} dS(\mathbf{x}), \quad (\text{B.2})$$

(but it is not the area itself, notice the constant). The third Minkowski functional is proportional to the integrated mean curvature  $C$  of the boundary:

$$V_2(\phi_0) = \frac{1}{6\pi} \int_{\delta F_{\phi_0}} \left( \frac{1}{R_1(\mathbf{x})} + \frac{1}{R_2(\mathbf{x})} \right) dS(\mathbf{x}), \quad (\text{B.3})$$

where  $R_1(\mathbf{x})$  and  $R_2(\mathbf{x})$  are the principal radii of curvature of the boundary. The fourth Minkowski functional is proportional to the integrated Gaussian curvature (the Euler characteristic) of the boundary:

$$V_3(\phi_0) = \frac{1}{4\pi} \int_{\delta F_{\phi_0}} \frac{1}{R_1(\mathbf{x})R_2(\mathbf{x})} dS(\mathbf{x}). \quad (\text{B.4})$$

At high (low) densities this functional gives us the number of isolated clumps (void bubbles) in the sample (Martínez & Saar 2002; Saar et al. 2007):

$$V_3 = N_{\text{clumps}} + N_{\text{bubbles}} - N_{\text{tunnels}}. \quad (\text{B.5})$$

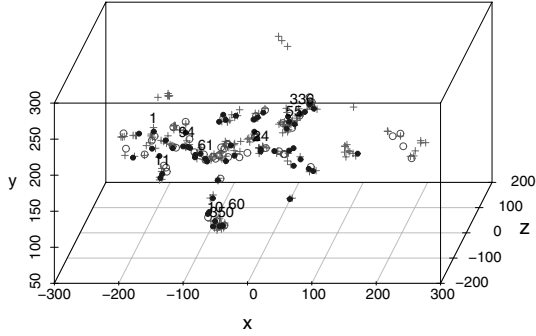


**Fig. C.1.** Distribution of groups with at least 12 member galaxies in our superclusters in the Cartesian coordinates as in Fig. 3, in units of  $h^{-1}$  Mpc. Filled circles denote the groups with at least 50 member galaxies, empty circles denote the groups with 30–49 member galaxies and crosses denote the groups with 12–29 member galaxies. The numbers show the ID's (Table 1, Col. 1) of very rich superclusters from Sect. 4.3.

As the argument labelling the isodensity surfaces, we chose the (excluded) mass fraction  $mf$  – the ratio of the mass in the regions with the density *lower* than the density at the surface, to the total mass of the supercluster. When this ratio runs from 0 to 1, the iso-surfaces move from the outer limiting boundary into the centre of the supercluster, i.e., the fraction  $mf = 0$  corresponds to the whole supercluster, and  $mf = 1$  – to its highest density peak.

We used directly only the fourth Minkowski functional in this paper; the other functionals were used to calculate the shapefinders (Sahni et al. 1998; Shandarin et al. 2004; Saar 2009). The shapefinders are defined as a set of combinations of Minkowski functionals:  $H_1 = 3V/S$  (thickness),  $H_2 = S/C$  (width), and  $H_3 = C/4\pi$  (length). The shapefinders have dimensions of length and are normalized to give  $H_i = R$  for a sphere of radius  $R$ . For smooth (ellipsoidal) surfaces, the shapefinders  $H_i$  follow the inequalities  $H_1 \leq H_2 \leq H_3$ . Oblate ellipsoids (pancakes) are characterised by  $H_1 \ll H_2 \approx H_3$ , while prolate ellipsoids (filaments) are described by  $H_1 \approx H_2 \ll H_3$ .

Sahni et al. (1998) also defined two dimensionless shapefinders  $K_1$  (planarity) and  $K_2$  (filamentarity):  $K_1 = (H_2 - H_1)/(H_2 + H_1)$  and  $K_2 = (H_3 - H_2)/(H_3 + H_2)$ .

In the  $(K_1, K_2)$ -plane filaments are located near the  $K_2$ -axis, pancakes near the  $K_1$ -axis, and ribbons along the diameter, connecting the spheres at the origin with the ideal ribbon at (1, 1). In Einasto et al. (2007d) we calculated typical morphological signatures of a series of empirical models that serve as morphological templates to compare with the characteristic curves for superclusters in the  $(K_1, K_2)$ -plane.

### Appendix C: 3D figures of superclusters

Here we show the 3D distribution of groups in our superclusters. Figure C.1 is 3D presentation of Fig. 3 and shows the distribution of groups with at least twelve member galaxies in our superclusters in the Cartesian coordinates defined in Section 4.1, in units of  $h^{-1}$  Mpc. The filled circles denote groups with at least 50 member galaxies, empty circles denote groups with 30–49 member galaxies and crosses denote groups with 12–29 member galaxies. The numbers are ID numbers of superclusters with at least 950 member galaxies. Figures C.2, C.4, and C.4 show 3D distribution of groups in superclusters. In these figures we plot rich groups with at least 30 member galaxies with filled circles, groups with 2–29 member galaxies with empty

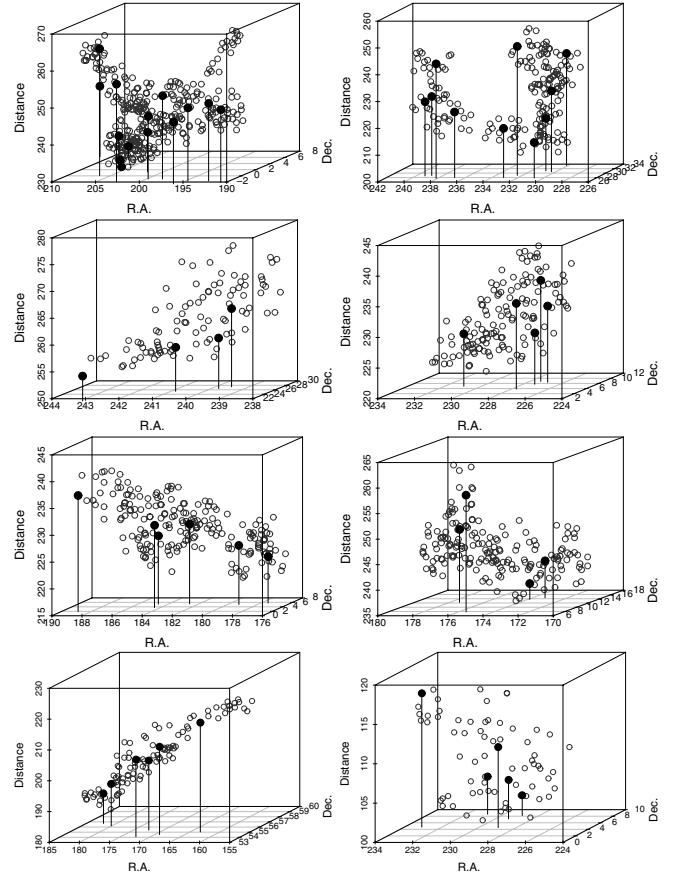


**Fig. C.2.** 3D figures of the very rich superclusters described in Sect. 4.3. Filled circles show the location of rich groups and clusters with at least 30 member galaxies, empty circles show poorer groups. We plot the right ascension (in degrees), declination (in degrees), and distance (in Mpc/h) of groups. Plots of superclusters are given in the same order as they are presented in the text. *From top to bottom*: left: the supercluster SC1 061, right: SC1 094, left: the supercluster SC1 001, right: SC1 011, left: the supercluster SC1 024, right: SC1 055, left: the supercluster SC1 336, right: SC1 350.

circles. We do not show the figures for superclusters, for which the value of the fourth Minkowski functional  $V_3 = 1$  over the whole mass fraction interval.

### Appendix D: The distribution of galaxies and rich groups in the sky and the fourth Minkowski functional and morphological signature for superclusters with less than 950 member galaxies

In this section we present the distribution of galaxies and rich groups/clusters in the sky as well as the fourth Minkowski functionals and morphological signatures for superclusters with less than 950 member galaxies (Figs. D.1–D.3). In all figures the left panels show the distribution of galaxies in the sky (dots). Circles in these panels mark the location of groups with at least 30 member galaxies. The size of a circle is proportional to the size of a group in the sky. The middle panels show the fourth Minkowski functional  $V_3$  vs. the mass fraction  $mf$ , and the right panels show the shapefinders  $K_1$  (planarity) and  $K_2$  (filamentarity) for the supercluster (the morphological signature). Filled circles in the right panels mark the value of the mass fraction  $mf = 0.7$ . In

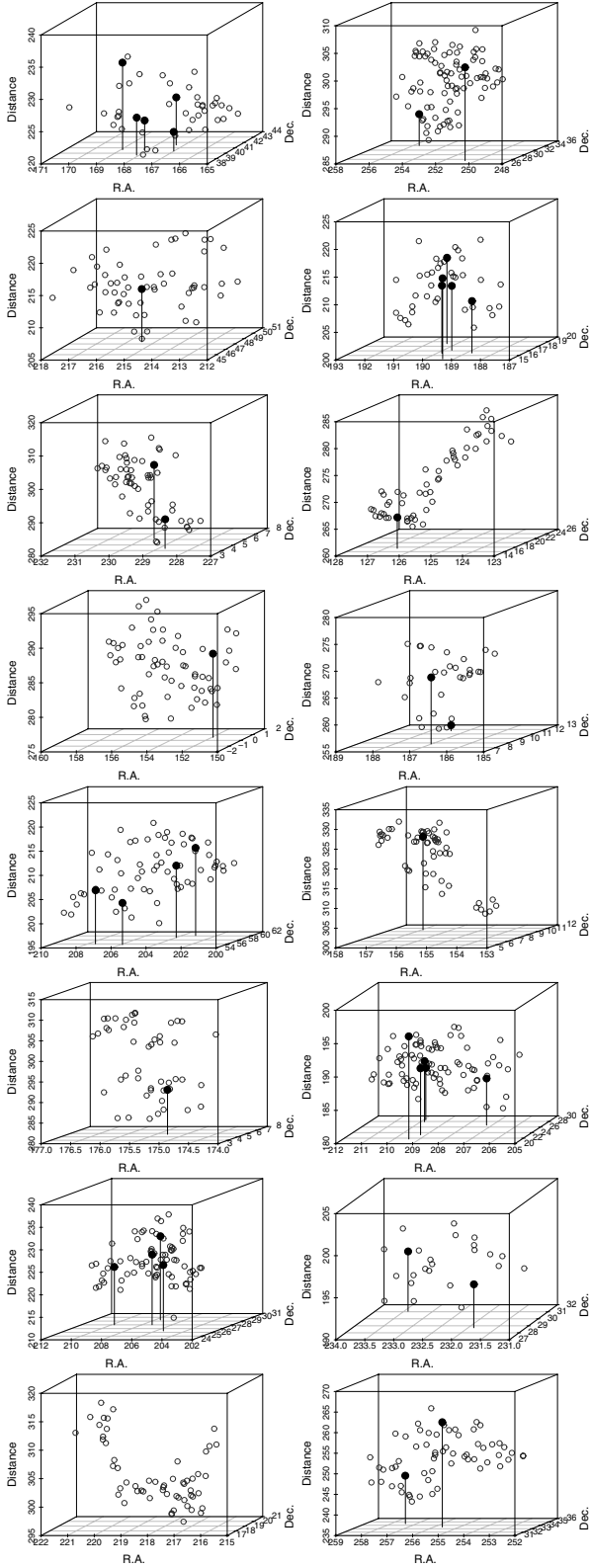


**Fig. C.3.** 3D figures of superclusters with less than 950 member galaxies. Panels and notations in this figure are the same as in Fig. C.2. *From top to bottom:* left: the supercluster SCI 038, right: SCI 064, left: the supercluster SCI 087, right: SCI 136, left: the supercluster SCI 152, right: SCI 189, left: the supercluster SCI 198, right: SCI 223, left: the supercluster SCI 228, right: SCI 317, left: the supercluster SCI 332, right: SCI 349, left: the supercluster SCI 351, right: SCI 362, left: the supercluster SCI 366, right: SCI 376.

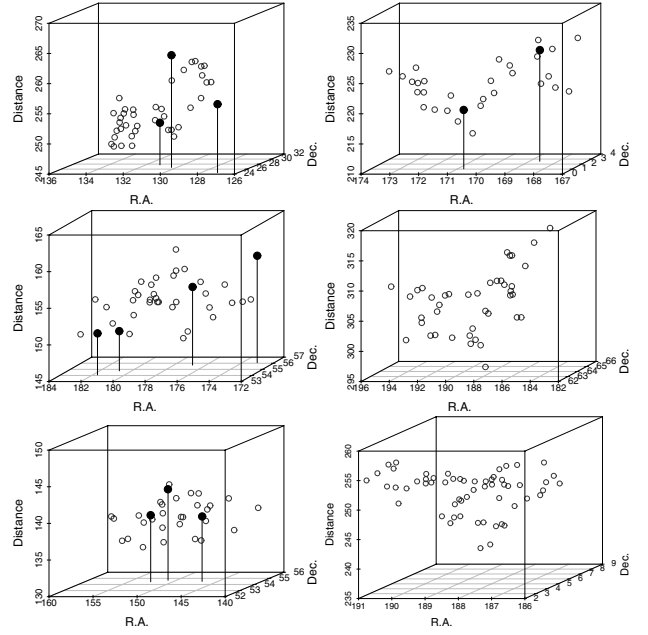


**Fig. C.4.** 3D figures of superclusters with less than 950 member galaxies (continued). Panels and notations in this figure are the same as in Fig. C.2. *From top to bottom:* left: the supercluster SCI 474, right: SCI 512, left: the supercluster SCI 525, right: SCI 530, left: the supercluster SCI 779, right: SCI 827.

the right panels the mass fraction increases anti-clockwise along the curves. As in the previous section, we do not show the figures for superclusters, for which the value of the fourth Minkowski functional  $V_3 = 1$  over the whole mass fraction interval.

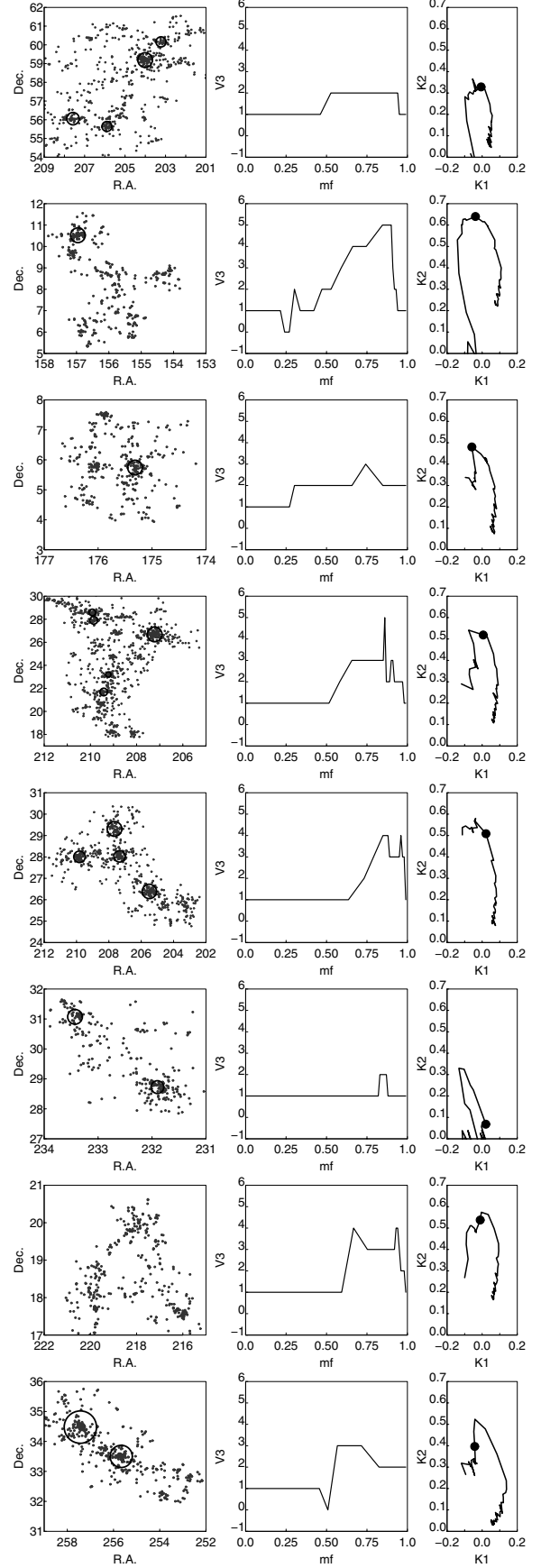
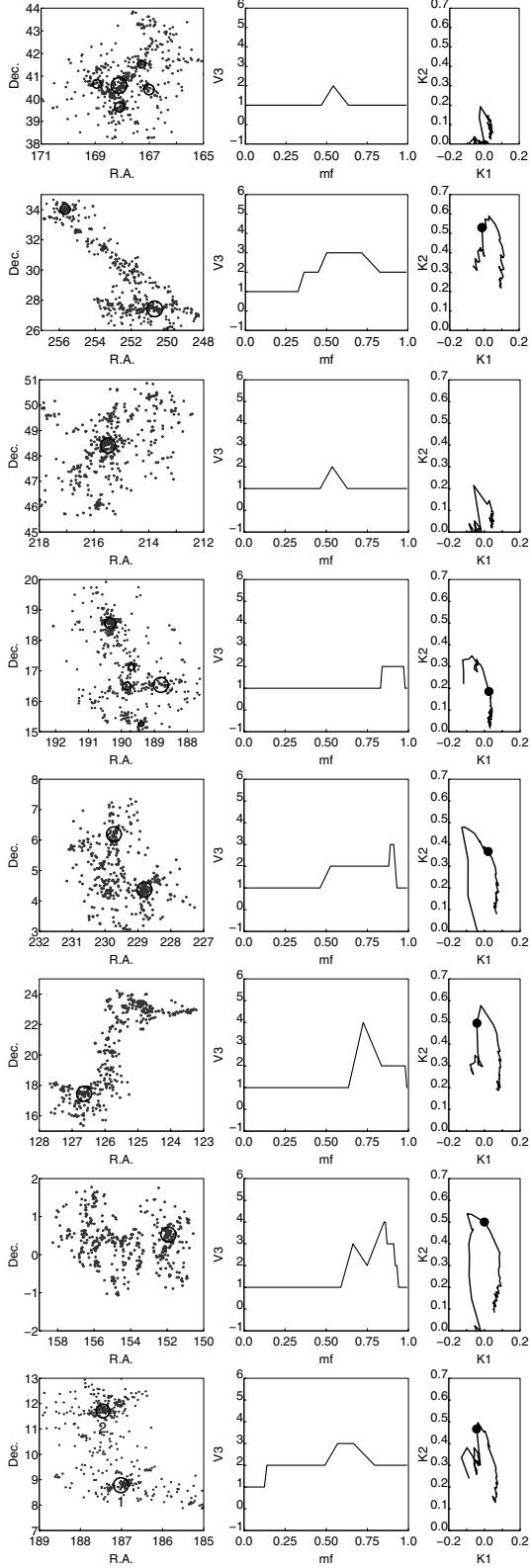


**Fig. D.1.** Left panels show the distribution of galaxies (dots) in the sky. Circles mark the location of groups with at least 30 member galaxies, and the size of a circle is proportional to the size of a group in the sky. The middle panels show the fourth Minkowski functional  $V_3$  vs. the mass fraction  $mf$ , and the right panels show the shapefinders  $K_1$  (planarity) and  $K_2$  (filamentarity) (the morphological signature). In the right panels filled circles mark the value of the mass fraction  $mf = 0.7$ ; the mass fraction increases anti-clockwise along the curves. From top to bottom: the superclusters SCI 1038, SCI 064, SCI 087, SCI 136, SCI 152, SCI 189, SCI 198, and SCI 223.

**Fig. D.2.** Panels in this figure are the same as in Fig. D.1. From top to bottom: the superclusters SCI 228, SCI 317, SCI 332, SCI 349, SCI 351, SCI 362, SCI 366, and SCI 376.

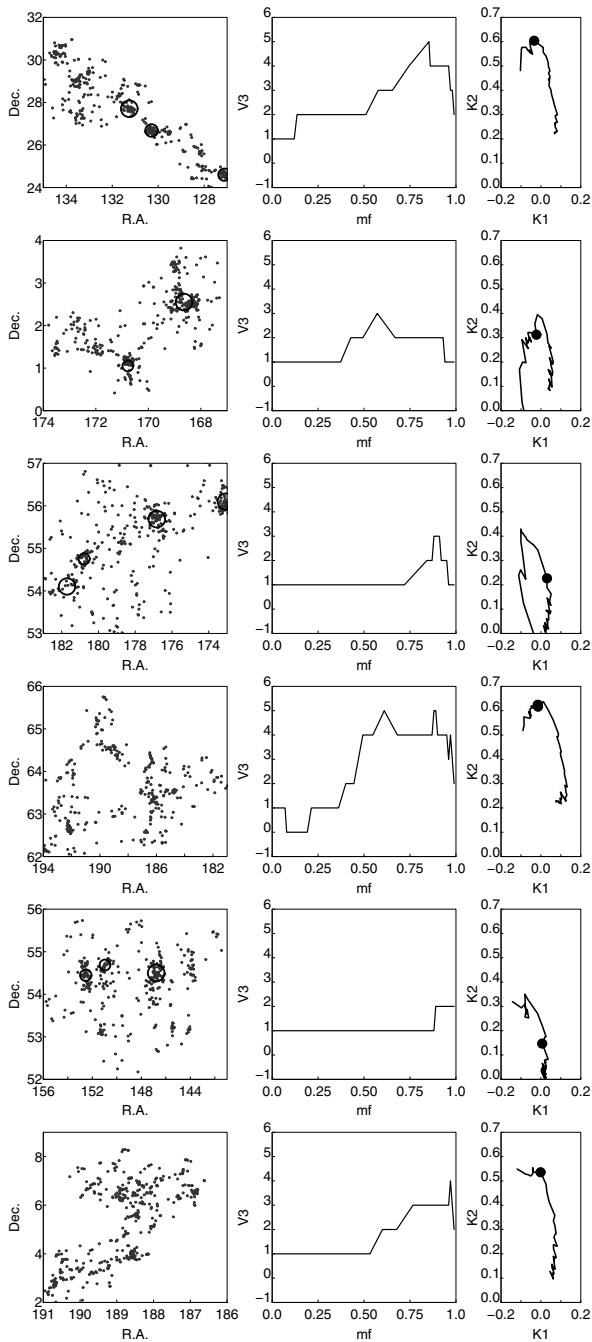


**Fig. D.3.** Panels in this figure are the same as in Fig. D.1. From top to bottom: the superclusters SCI 474, SCI 512, SCI 525, SCI 530, SCI 779, and SCI 827.

## References

- Abazajian, K. N., Adelman-McCarthy, J. K., Agüeros, M. A., et al. 2009, *ApJS*, 182, 543  
 Adelman-McCarthy, J. K., Agüeros, M. A., Allam, S. S., et al. 2008, *ApJS*, 175, 297  
 Aragón-Calvo, M. A., van de Weygaert, R., & Jones, B. J. T. 2010, *MNRAS*, 408, 2163  
 Araya-Melo, P. A., Reisenegger, A., Meza, A., et al. 2009, *MNRAS*, 399, 97  
 Bardelli, S., Zucca, E., Zamorani, G., Moscardini, L., & Scaramella, R. 2000, *MNRAS*, 312, 540  
 Basilakos, S. 2003, *MNRAS*, 344, 602  
 Belsole, E., Pratt, G. W., Sauvageot, J., & Bourdin, H. 2004, *A&A*, 415, 821  
 Bharadwaj, S., Bhavsar, S. P., & Sheth, J. V. 2004, *ApJ*, 606, 25  
 Blanton, M. R., & Roweis, S. 2007, *AJ*, 133, 734

- Blanton, M. R., Brinkmann, J., Csabai, I., et al. 2003a, *AJ*, 125, 2348  
 Blanton, M. R., Hogg, D. W., Bahcall, N. A., et al. 2003b, *ApJ*, 592, 819  
 Böhringer, H., Schuecker, P., Guzzo, L., et al. 2004, *A&A*, 425, 367  
 Bond, J. R., Kofman, L., & Pogosyan, D. 1996, *Nature*, 380, 603  
 Bond, N. A., Strauss, M. A., & Cen, R. 2010, *MNRAS*, 409, 156  
 Buote, D. A., Zappacosta, L., Fang, T., et al. 2009, *ApJ*, 695, 1351  
 Ceccarelli, L., Padilla, N., & Lambas, D. G. 2008, *MNRAS*, 390, L9  
 Chatzikos, M., Sarazin, C. L., & Kempner, J. C. 2006, *ApJ*, 643, 751  
 Colless, M., Peterson, B. A., Jackson, C., et al. 2003  
 [arXiv:astro-ph/0306581]  
 Costa-Duarte, M. V., Sodré, Jr., L., & Durret, F. 2011, *MNRAS*, 411, 1716  
 de Lapparent, V., Geller, M. J., & Huchra, J. P. 1986, *ApJ*, 302, L1  
 Einasto, J. 2010, in *Am. Inst. Phys. Conf. Ser.* 1205, ed. R. Ruffini, & G. Vereshchagin, 72  
 Einasto, J., Joeveer, M., & Saar, E. 1980, *MNRAS*, 193, 353  
 Einasto, M., Einasto, J., Tago, E., Dalton, G. B., & Andernach, H. 1994, *MNRAS*, 269, 301  
 Einasto, J., Einasto, M., Gottlöber, S., et al. 1997a, *Nature*, 385, 139  
 Einasto, M., Tago, E., Jaaniste, J., Einasto, J., & Andernach, H. 1997b, *A&AS*, 123, 119  
 Einasto, M., Einasto, J., Tago, E., Müller, V., & Andernach, H. 2001, *AJ*, 122, 2222  
 Einasto, J., Hütsi, G., Einasto, M., et al. 2003a, *A&A*, 405, 425  
 Einasto, M., Jaaniste, J., Einasto, J., et al. 2003b, *A&A*, 405, 821  
 Einasto, J., Einasto, M., Saar, E., et al. 2006, *A&A*, 459, L1  
 Einasto, J., Einasto, M., Saar, E., et al. 2007a, *A&A*, 462, 397  
 Einasto, J., Einasto, M., Tago, E., et al. 2007b, *A&A*, 462, 811  
 Einasto, M., Einasto, J., Tago, E., et al. 2007c, *A&A*, 464, 815  
 Einasto, M., Saar, E., Liivamägi, L. J., et al. 2007d, *A&A*, 476, 697  
 Einasto, M., Saar, E., Martínez, V. J., et al. 2008, *ApJ*, 685, 83  
 Einasto, M., Tago, E., Saar, E., et al. 2010, *A&A*, 522, A92  
 Einasto, M., Liivamägi, L. J., Tempel, E., et al. 2011, *ApJ*, accepted  
 [arXiv:1105.1632]  
 Erdoğan, P., Lahav, O., Zaroubi, S., et al. 2004, *MNRAS*, 352, 939  
 Fleenor, M. C., & Johnston-Hollitt, M. 2010, in *ASP Conf. Ser.* 423, ed. B. Smith, J. Higdon, S. Higdon, & N. Bastian, 81  
 Fraley, C., & Raftery, A. E. 2006, Technical Report, Dep. of Statistics, University of Washington, 504, 1  
 Gal, R. R., Lemaux, B. C., Lubin, L. M., Kocevski, D., & Squires, G. K. 2008, *ApJ*, 684, 933  
 Gaztanaga, E., & Maehoenen, P. 1996, *ApJ*, 462, L1  
 Génova-Santos, R., Rubiño-Martín, J. A., Rebolo, R., et al. 2005, *MNRAS*, 363, 79  
 Génova-Santos, R., Rubiño-Martín, J. A., Rebolo, R., et al. 2008, *MNRAS*, 391, 1127  
 Génova-Santos, R., Padilla-Torres, C. P., Rubiño Martín, J. A., Gutiérrez, C. M., & Rebolo, R. 2010, *MNRAS*, 403, 1531  
 Gott, J. R. I., Jurić, M., Schlegel, D., et al. 2005, *ApJ*, 624, 463  
 Gott, J. R. I., Hambrick, D. C., Vogeley, M. S., et al. 2008, *ApJ*, 675, 16  
 Gramann, M., & Suhhonenko, I. 2002, *MNRAS*, 337, 1417  
 Gregory, S. A., & Thompson, L. A. 1978, *ApJ*, 222, 784  
 Haines, C. P., Merluzzi, P., Mercurio, A., et al. 2006, *MNRAS*, 371, 55  
 Heymans, C., Gray, M. E., Peng, C. Y., et al. 2008, *MNRAS*, 385, 1431  
 Hoffman, Y., Lahav, O., Yepes, G., & Dover, Y. 2007, *J. Cosmology Astropart. Phys.*, 10, 16  
 Hütsi, G. 2010, *MNRAS*, 401, 2477  
 Ihaka, R., & Gentleman, R. 1996, *J. Comp. Graph. Stat.*, 5, 299  
 Jaaniste, J., Tago, E., Einasto, M., et al. 1998, *A&A*, 336, 35  
 Joeveer, M., Einasto, J., & Tago, E. 1978, *MNRAS*, 185, 357  
 Kofman, L. A., Einasto, J., & Linde, A. D. 1987, *Nature*, 326, 48  
 Kolokotronis, V., Basilakos, S., & Plionis, M. 2002, *MNRAS*, 331, 1020  
 Kopylova, F. G., & Kopylov, A. I. 2009, *Astrophys. Bull.*, 64, 1  
 Lietzen, H., Heinämäki, P., Nurmi, P., et al. 2009, *A&A*, 501, 145  
 Liivamägi, L. J., Tempel, E., & Saar, E. 2010 [arXiv:1012.1989]  
 Luparello, H. E., Lares, M., Lambas, D. G., & Padilla, N. D. 2011, *MNRAS*, accepted [arXiv:1101.1961]  
 Markevitch, M., Ponman, T. J., Nulsen, P. E. J., et al. 2000, *ApJ*, 541, 542  
 Martínez, V. J., & Saar, E. 2002, *Statistics of the Galaxy Distribution (Boca Raton: Chapman & Hall/CRC)*  
 Martínez, V. J., Arnalte-Mur, P., Saar, E., et al. 2009, *ApJ*, 696, L93  
 Mobasher, B., Dickinson, M., Ferguson, H. C., et al. 2005, *ApJ*, 635, 832  
 Moles, M., Benítez, N., Aguerri, J. A. L., et al. 2008, *AJ*, 136, 1325  
 Nakata, F., Kodama, T., Shimasaku, K., et al. 2005, *MNRAS*, 357, 1357  
 Nichol, R. C., Sheth, R. K., Suto, Y., et al. 2006, *MNRAS*, 368, 1507  
 Noh, Y., & Cohn, J. D. 2011, *MNRAS*, submitted  
 Oort, J. H. 1983, *ARA&A*, 21, 373  
 Ouchi, M., Shimasaku, K., Akiyama, M., et al. 2005, *ApJ*, 620, L1

- Padilla-Torres, C. P., Gutiérrez, C. M., Rebolo, R., Génova-Santos, R., & Rubiño-Martin, J. A. 2009, MNRAS, 396, 53
- Padilla-Torres, C. P., Rebolo, R., Gutiérrez, C. M., Génova-Santos, R., & Rubiño-Martin, J. A. 2010, in *Highlights of Spanish Astrophysics V*, ed. J. M. Diego, L. J. Goicoechea, J. I. González-Serrano, & J. Gorgas, 329
- Park, C., Choi, Y., Vogeley, M. S., Gott, III, J. R., & Blanton, M. R. 2007, ApJ, 658, 898
- Pimblet, K. A., Andernach, H., Fishlock, C. K., Roseboom, I. G., & Owers, M. S. 2011, MNRAS, 410, 1837
- Planck Collaboration, Ade, P. A. R., Aghanim, N., Arnaud, M., et al. 2011, A&A, accepted [[arXiv:1101.2024](https://arxiv.org/abs/1101.2024)]
- Plionis, M. 2004, in *Outskirts of Galaxy Clusters: Intense Life in the Suburbs*, ed. A. Diaferio, IAU Colloq., 195, 19
- Porter, S. C., Raychaudhury, S., Pimblet, K. A., & Drinkwater, M. J. 2008, MNRAS, 388, 1152
- Rose, J. A., Gaba, A. E., Christiansen, W. A., et al. 2002, AJ, 123, 1216
- Saar, E. 2009, in *Data Analysis in Cosmology*, ed. V. J. Martínez, E. Saar, E. Martínez-Gonzalez, & M.-J. Pons-Bordería (Berlin: Springer-Verlag), 523
- Saar, E., Martínez, V. J., Starck, J., & Donoho, D. L. 2007, MNRAS, 374, 1030
- Sahni, V., Sathyaprakash, B. S., & Shandarin, S. F. 1998, ApJ, 495, L5
- Sathyaprakash, B. S., Sahni, V., & Shandarin, S. 1998, ApJ, 508, 551
- Schirmer, M., Hildebrandt, H., Kuijken, K., & Erben, T. 2011, A&A, accepted [[arXiv:1102.4617](https://arxiv.org/abs/1102.4617)]
- Schmalzing, J., & Buchert, T. 1997, ApJ, 482, L1
- Shandarin, S. F., Sheth, J. V., & Sahni, V. 2004, MNRAS, 353, 162
- Sheth, J. V., Sahni, V., Shandarin, S. F., & Sathyaprakash, B. S. 2003, MNRAS, 343, 22
- Silverman, B. W. 1986, *Density Estimation for Statistics and Data Analysis* (Boca Raton: Chapman & Hall, CRC Press)
- Small, T. A., Ma, C., Sargent, W. L. W., & Hamilton, D. 1998, ApJ, 492, 45
- Sousbie, T. 2011, MNRAS, submitted
- Sousbie, T., Pichon, C., & Kawahara, H. 2011, MNRAS, submitted
- Stoica, R. S., Martínez, V. J., & Saar, E. 2010, A&A, 510, A38
- Swinbank, A. M., Edge, A. C., Smail, I., et al. 2007, MNRAS, 379, 1343
- Tago, E., Saar, E., Tempel, E., et al. 2010, A&A, 514, A102
- Tanaka, M., Finoguenov, A., Kodama, T., et al. 2009, A&A, 505, L9
- Tempel, E., Einasto, J., Einasto, M., Saar, E., & Tago, E. 2009, A&A, 495, 37
- Tempel, E., Saar, E., Liivamägi, L. J., et al. 2011, A&A, 529, A53
- Venemans, B. P., Röttgering, H. J. A., Overzier, R. A., et al. 2004, A&A, 424, L17
- Vogele, M. S., Hoyle, F., Rojas, R. R., & Goldberg, D. M. 2004, in *Outskirts of Galaxy Clusters: Intense Life in the Suburbs*, ed. A. Diaferio, IAU Colloq., 195, 5
- Wolf, C., Gray, M. E., & Meisenheimer, K. 2005, A&A, 443, 435
- Zappacosta, L., Maiolino, R., Finoguenov, A., et al. 2005, A&A, 434, 801
- Zeldovich, I. B., Einasto, J., & Shandarin, S. F. 1982, Nature, 300, 407
- Zucca, E., Zamorani, G., Scaramella, R., & Vettolani, G. 1993, ApJ, 407, 470